GIScience & Remote Sensing

ISSN: (Print) (Online) Journal homepage: www.tandfonline.com/journals/tgrs20

Enhancing urban resilience through Tomo-PSInSAR-based structural health monitoring

Yi-Ching Chen, Yunung Nina Lin, Tee-Ann Teo, Chin-Yeh Chen, Tian-Yuan Shih & Hsin Tung

To cite this article: Yi-Ching Chen, Yunung Nina Lin, Tee-Ann Teo, Chin-Yeh Chen, Tian-Yuan Shih & Hsin Tung (2025) Enhancing urban resilience through Tomo-PSInSAR-based structural health monitoring, GIScience & Remote Sensing, 62:1, 2482329, DOI: 10.1080/15481603.2025.2482329

To link to this article: https://doi.org/10.1080/15481603.2025.2482329

Published online: 25 Mar 2025.

GISCIENCE & REMOTE SENSING
2025, VOL. 62, NO. 1, 2482329
https://doi.org/10.1080/15481603.2025.2482329

Taylor & Francis
Taylor & Francis Group

Enhancing urban resilience through Tomo-PSInSAR-based structural health monitoring

Yi-Ching Chen[a]*, Yunung Nina Lin[a], Tee-Ann Teo[b], Chin-Yeh Chen[a], Tian-Yuan Shih[b] and Hsin Tung[a]

[a]Institute of Earth Sciences, Academia Sinica, Taipei, Taiwan; [b]Department of Civil Engineering, National Yang Ming Chiao Tung University, Hsinchu, Taiwan

ABSTRACT

Structural health monitoring (SHM) is crucial for aging buildings, especially in areas with frequent seismic activities, but the cost is often prohibitive for most private property owners. This study explores the feasibility of large-scale SHM using tomographic persistent-scatterer interferometric synthetic aperture radar (Tomo-PSInSAR) within an urban planning context. By applying Tomo-PSInSAR to TerraSAR-X/TanDEM-X data over the Taipei Basin, a workflow is developed to assess building settlement and tilt rates. The analysis identifies 11.6% of building polygons as eligible for SHM, with 10.8% of these showing anomalous deformation. Peak settlement and tilting rates reach −14 mm/yr and 1/760 yr^{-1}, respectively. Among buildings within urban regeneration plans, 9.4% are eligible for analysis, with 11.9% of them exhibiting deformation anomalies. Building age and soil properties partially explain variability in deformation anomalies, but additional factors are needed to fully account for it. For instance, the high deformation anomalies observed in buildings aged 30–50 years may be attributed to poor construction quality and the use of inadequate materials, such as sea sand in concrete. Several key factors affecting SAR-based SHM performance are identified: insufficient scatterers, uneven scatterer spatial distribution, the absence or geometric inaccuracy of building polygons, and missing age information. These limitations can be addressed through integrating SAR data from multiple viewing geometries, increasing acquisitions, and developing closer collaboration with government agencies.

ARTICLE HISTORY
Received 24 August 2024
Accepted 17 March 2025

KEYWORDS
Tomo-PSInSAR; TerraSAR-X/TanDEM-X; structural health monitoring; resilient urban planning; urban regeneration; building orientation

1. Introduction

Over the past century, cities around the globe have experienced rapid and unprecedented growth. Today, 55% of the world's population reside in urban areas, a figure projected to rise to 68% by 2050 (United Nations and Population Division 2019). With the sharp increase in demand and, in some cases, inadequate regulations and practices, the quality of construction can vary. Historical data on building collapses over the past 125 years reveal that structural failure – including faulty design, construction, renovation, mechanical errors, and fatigue failure – accounts for 47% of the 152 reported incidents (Figure 1(a)). This issue has become increasingly prevalent over time, particularly since the 2000s, with 17 structural failures reported between 2010 and 2019, and 15 between 2020 and 2024 (Figure 1(b)). The spike in cases at the start of the 21st century may be attributed to more advanced methods of news dissemination, and/or the aging of buildings constructed in the previous century. Structural failure is not an issue confined to developing nations; it is equally common in developed countries, such as in North America and Europe (Figure 1(c)). One of the most notable recent examples is the 2021 Champlain Towers South collapse in Florida, which resulted in 98 deaths and 11 injuries. Initial investigations suggest that the collapse was caused by a combination of structural failures due to multiple factors occurring simultaneously (https://en.wikipedia.org/wiki/Surfside_condominium_collapse, last accessed on August 2024).

Building collapses due to structural failure, as opposed to those caused by force majeure factors like weather, earthquakes, mass movement, or conflicts, often provoke greater social outrage and unrest. This is because such tragedies are theoretically preventable. In many instances, the total economic loss far exceeds the compensation available through all

CONTACT Yunung Nina Lin ninalin@earth.sinica.edu.tw
*Present address: Viridien (formerly CGG) Satellite Mapping, Edenbridge, Kent, UK.

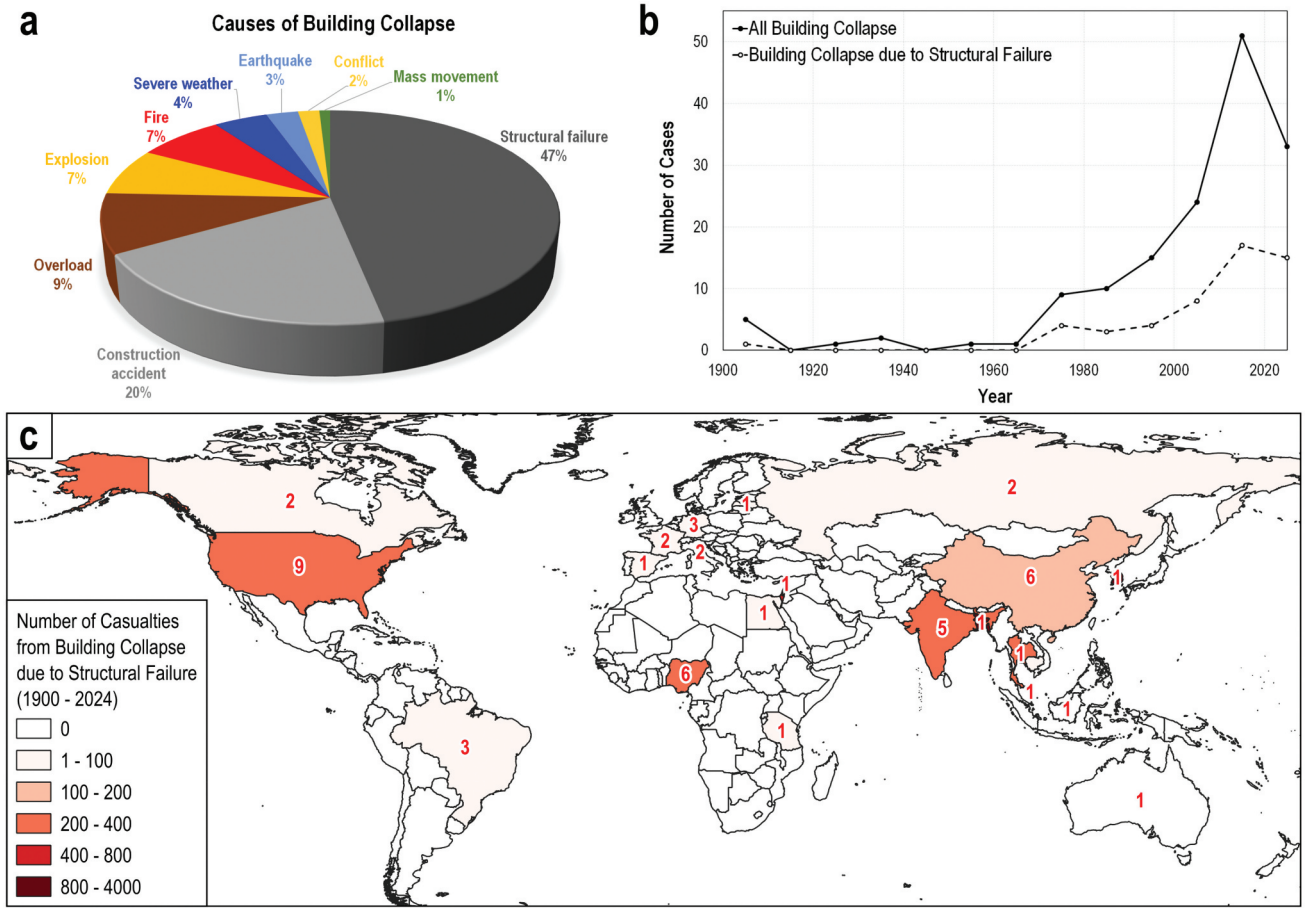

Figure 1. Causes, temporal trends and spatial distribution of building collapses worldwide. Source of data:https://en.Wikipedia.org/wiki/List_of_building_and_structure_collapses (last accessed in August 2024). (a) Causes of building collapse from a list of 152 reported cases between 1900 and 2024. (b) Temporal trends of reported building collapses, including those due to structural failure. (c) Spatial distribution of casualties associated with building collapse cases resulting from structural failure. Red numbers indicate the number of collapse cases.

kinds of claims (for example, https://ww3.rics.org/uk/en/modus/business-and-skills/surveying-stories/champlain-towers–valuation-in-the-aftermath-of-tragedy.html, last accessed in August 2024). These societal and economic impacts underscore the importance of adequate and safe housing, which is a primary objective of the 11th Sustainable Development Goal, focusing on sustainable cities and communities (SDG 11, https://www.undp.org/sustainable-development-goals/sustainable-cities-and-communities, last accessed in June 2024).

Achieving adequate and safe housing for everyone requires a focus on resilient urban planning. Urban planning is a complex, multidimensional process that seeks to guide the physical, social, economic, and environmental development of cities. It entails crafting a vision for a city's future and implementing strategies such as land-use planning, zoning, infrastructure development, housing provision, and cultural heritage preservation (Pacione 2005). Urban resilience complements urban planning by enhancing a city's ability to anticipate, adapt to, and recover from shocks and stressors. It involves preparing for potential threats, mitigating impacts, rebuilding after a crisis, and adaption to long-term changes (Chmutina, Ganor, and Bosher 2014; Sharifi and Yamagata 2014). By integrating resilience into urban planning, cities can proactively address risks and improve their recovery capabilities. In this respect, the United Nations' *Crisis Resilient Urban Futures* report offers valuable guidelines for fostering urban resilience. Among them, strengthening infrastructure and buildings to withstand natural disasters and climate change is considered crucial for protecting lives, property, and essential services during extreme events (Economic and Social Commission for Asia and the Pacific 2023).

A vital tool for identifying buildings and infrastructure at risk is structural health monitoring (SHM). SHM involves collecting, interpreting, and analyzing data from structures to assess their health status and estimate their remaining life span. This process also supports informed decision regarding rehabilitation and retrofitting efforts (Balageas, Fritzen, and Güemes 2006). Despite significant advancements in SHM techniques over the past decades, several challenges remain. Since SHM usually requires installing instruments at specific locations on structures, issues such as site accessibility, environmental constraints, device maintenance, and data transmission frequently arise. Moreover, the time and financial costs often hinder its widespread adoption (Rai 2024). However, with urban area expanding at a global average annual rate of 1.8% – and even faster in developing countries (United Nations and Population Division 2019) – scalable and cost-effective SHM solutions will be helpful in alleviating the rising cost of urban building and infrastructure maintenance, enabling better management of resilience (Gielen et al. 2019).

Over the past decade, the growth of active and passive satellite missions has demonstrated the potential of remote sensing to provide large-scale, cost-effective solutions for addressing vulnerabilities in urban areas. The scope of application includes urban heat island effect, slums and informal settlements, urban floods, green space, and carbon-dioxide emissions (Wellmann et al. 2020; Zhu et al. 2019). Insights from remote sensing-based studies have even informed actionable management strategies (Katz and Batterman 2019; Yu et al. 2012). For monitoring man-made structures, satellite-borne synthetic aperture radar (SAR) systems have become increasingly valuable due to their ability to acquire images and detect deformation signals in a large area regardless of weather conditions or time of day (Fornaro and Pascazio 2014). For instance, before the collapse of the Champlain Towers South, multi-temporal interferometric synthetic aperture radar (MTInSAR) observations detected ongoing deformation at a rate of ~2 mm/yr (Fiaschi and Wdowinski 2020).

One widely used MTInSAR technique for monitoring manmade structures is persistent scatterer interferometry (PSInSAR). Developed in the early 2000s, PSInSAR is designed to measure surface deformation by analyzing persistent scatterers (PSs) in a series of images acquired with the same geometry (Ferretti, Prati, and Rocca 2000; Hooper et al. 2004; Hooper, Segall, and Zebker 2007). This technique has been particularly successful in monitoring structures within urban areas, where persistent scatterers are abundant. PSInSAR has been employed to identify issues from local-scale, tunneling-induced building deformation (Giardina et al. 2019; Macchiarulo et al. 2021), to medium- and large-scale, settlement-induced deformation (Cerchiello et al. 2017; Drougkas et al. 2020a, b; Giardina et al. 2019; Macchiarulo et al. 2021). When integrated with machine learning and probabilistic models, PSInSAR results can enhance the detection of infrastructure failures and the identification of risk zones, providing critical information for urban managers (Rodríguez-Antuñano et al. 2022, 2023, 2024).

Despite the popularity in man-made structure monitoring, PSInSAR faces certain challenges when applied to SHM. One challenge is the assumption that each resolution cell contains a single scatterer, which limits the number of usable scatterers for assessing the deformation of individual buildings. Another issue is the positioning of the scatterers: PS points are typically assigned to the center of each resolution cell, which may not accurately reflect their actual true locations and deformation velocities, leading to potential misinterpretation of results.

To address these challenges, tomographic synthetic aperture radar (TomoSAR), also known as SAR tomography, was introduced to resolve the ambiguities in scatterer numbers and positions within each resolution cell (Reigber and Moreira 2000). TomoSAR extends the concept of aperture synthesis to the third dimension – the elevation direction – which is perpendicular to the range-azimuth plane of a SAR image. A 2D SAR image can be considered a projection of actual 3D features observed from a specific sensing geometry, with each pixel representing the backscattered responses from one or more objects at the same distance from the sensor. By leveraging the multi-baseline approach, where the same object is observed from slightly different viewpoints across multiple tracks, TomoSAR reconstructs the complex reflectivity profile along the elevation direction. This capability allows TomoSAR to build 3D urban models from space (Fornaro and Pascazio 2014; Fornaro et al. 2012; Zhu and Bamler 2010a). Depending on the model complexity, TomoSAR can be further extended into a multi-dimensional model space, enabling the

estimation of geophysical properties such as the scatterers' line-of-sight (LOS) linear velocity and thermal expansion parameters (Zhu et al. 2016). Several studies have demonstrated TomoSAR's potential in conducting structural deformation analysis (Budillon and Schirinzi 2022; Ma et al. 2015).

Promising as TomoSAR's potential may be, most research has focused on the deformation of a limited number of selected buildings (Budillon and Schirinzi 2022; Chen et al. 2019; Ma and Lin 2016) or heritage sites (Chen et al. 2021). To date, there has been no systematic evaluation of the efficiency and effectiveness of TomoSAR in the broader context of urban planning. Specifically, while a comprehensive urban model can be reconstructed using more than 450 SAR images from multiple viewing geometries (Zhu et al. 2016), such extensive datasets are usually not available in most scenarios. There are two critical questions from the urban planning's perspective. First, what proportion of buildings with detectable deformation can be resolved if only a small fraction of the SAR data is available? Second, how to translate TomoSAR results into actionable insights for urban planners, who are more concerned with the overall structural deformation of *buildings* rather than the deformation velocities of individual *scatterers*?. Addressing these two questions is essential for integrating TomoSAR into large-scale SHM applications and making it a practical tool for urban planning and management.

To address the two questions mentioned above, detailed urban planning data and other relevant background information are needed. This study focuses on the Taipei Basin, where comprehensive information about private properties is accessible with necessary permissions (note: most of the data is not publicly accessible due to privacy concerns). Located in northern Taiwan, the Taipei Basin encompasses Taipei City and the surrounding New Taipei City, with a combined population of approximately 7 million people. Taipei City alone is home to 2.6 million residents and has a population density of 9,545 people/km^2 (2020 Population and Housing Census, National Statistics, https://eng.stat.gov.tw, last accessed in December 2024). The basin is characterized by a high-temperature, high-humidity environment and is frequently impacted by natural hazards such as typhoons, earthquakes, and volcanic activities. These conditions, coupled with a dense population, are similar to those faced by many large cities in Japan (and also in Southeast Asia). Consequently, both Taiwan and Japan have widely adopted reinforced concrete buildings to address their hazardous natural environment (Lee 2015). A unique challenge for Taipei is the wide-spread soft soil within the basin as a result of its geological history, which further increases the vulnerability of buildings and infrastructure during seismic events. Insights and lessons learned from large-scale SHM analysis in the Taipei Basin could therefore serve as a reference for cities with similar conditions.

In this work, we demonstrate the application of the Tomo-PSInSAR technique – a combination of TomoSAR and PSInSAR – for monitoring building deformation in Taipei. With the generous support of the TerraSAR-X science proposal from the German Aerospace Center (DLR), we gained access to 41 TerraSAR-X/TanDEM-X SAR archive images spanning 2.5 years. The TerraSAR-X and TanDEM-X satellites are equipped with precise orbit control and a sufficiently wide baseline distribution (nearly ±450 m), two essential factors for effectively forming the aperture in the elevation direction to enable tomography. The high spatial resolution (~3 m) of their stripmap images also makes it ideal for urban applications. We obtain scatterer velocities from these images and develop a workflow to extract building-level deformation, including settlement and tilting rates. We identify buildings exhibiting deformation anomalies across different factors, such as age groups and soil properties, followed by validation and field observations. We also evaluate the completeness of information from urban planning's perspective and discuss how to further improve the efficacy. Finally, we provide management recommendations regarding how to incorporate this tool into urban planning processes. The structure of this work is organized as follows: Section 2 details the methodology, Section 3 describes the study area and datasets used, Section 4 presents results and discussions, and Section 5 provides the conclusions.

2. Methodology

In this section, we will first introduce the Tomo-PSInSAR method, an MTInSAR approach used to extract scatterer velocities while performing 3D

scatterer positioning. Next, we describe the process of removing long-wavelength, ground-related signals from the Tomo-PSInSAR velocity field to isolate short-wavelength, building-related signals. Finally, we outline the workflow for identifying two types of building deformation: settlement and tilt.

2.1. Tomo-PSInSAR

The Tomo-PSInSAR method, introduced by Ma and Lin (2016), is a two-tier network approach that combines the strength of PSInSAR (reliable PS selection) and TomoSAR (ability to detect multiple scatterers within the same pixel and their 3D positions). By pre-selecting the eligible PS points for tomographic analysis, this method reduces the lengthy runtime typically required by conventional TomoSAR. Additionally, it allows the detection of PS points without the need to initially remove the atmospheric phase screen (APS). By adopting tomography along with an M-estimator, the scatterer velocity and elevation can be solved simultaneously and at a higher resolution.

The workflow (Figure 2) begins with image coregistration and differential interferometry, similar to the standard PSInSAR processing. Potential single PSs (SPSs) are then identified based on the amplitude dispersion index (Ferretti, Prati, and Rocca 2001). These SPSs, referred to as primary PS candidates (PPSCs), are connected using Delaunay triangulation

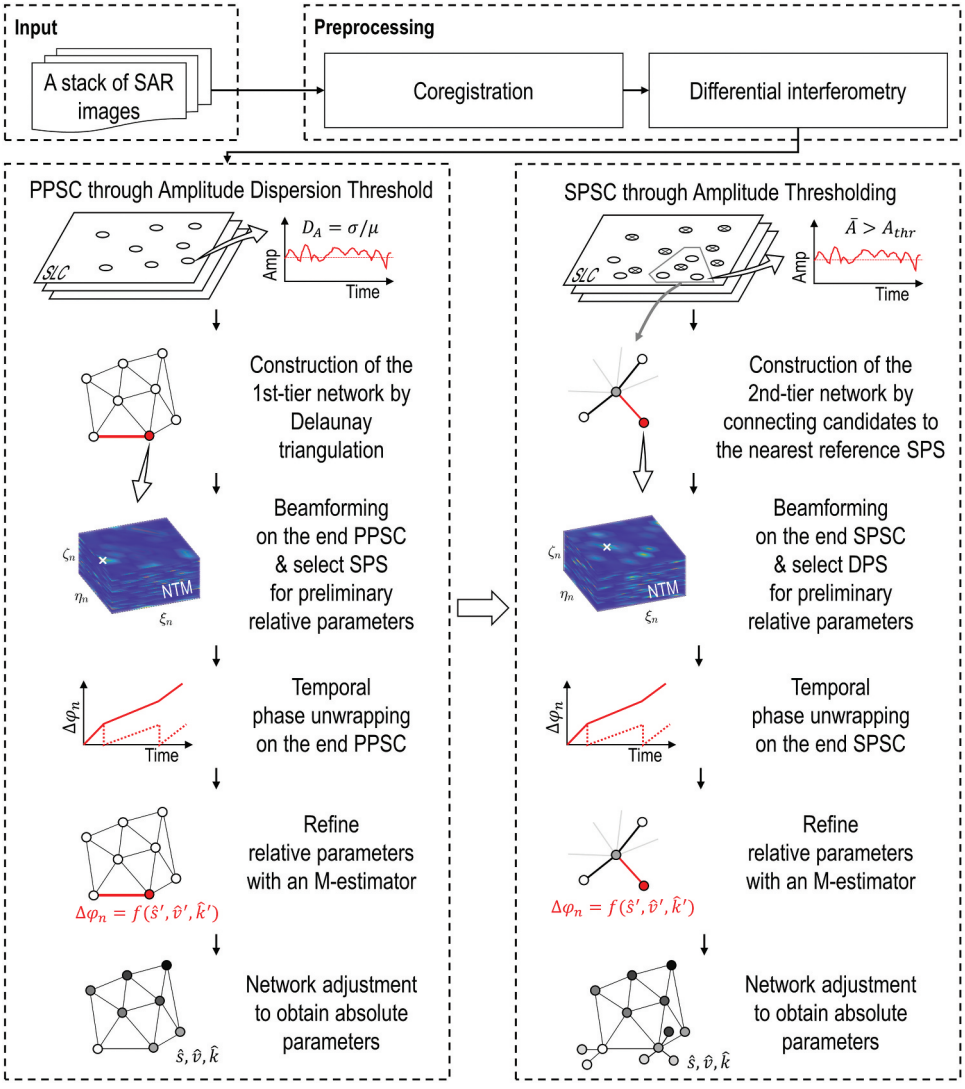

Figure 2. Flowchart of the Tomo-PSInSAR method. PPSC: primary PS candidate; SPS = single PS; SPSC: secondary PS candidate; DPS = double PS. M-estimator: referring to an iteratively reweighted least squares estimator (Ma and Lin 2016). See section 2.1 for more details.

to establish the first-tier network. For each arc formed between two PPSCs, one PPSC is designated as the start PPSC and the other as the end PPSC. By retaining only short arcs, APS effects can be mitigated by subtracting the phase of the start PPSC from the end PPSC. After this correction, tomography is performed on the end PPSC, with the details elaborated as follows.

Consider a repeat-pass SAR sensor that flies over the same area along N parallel tracks, each spatially separated from the reference track by B_n ($n = 1, \ldots, N$). The signal model for a pixel in the n-th acquisition can be expressed as (Reale, Fornaro, and Pauciullo 2013)

$$g_n = \int_{\Delta s}\int_{\Delta v}\int_{\Delta k} \gamma(s,v,k)\exp[j2\pi(\xi_n s + \eta_n v + \zeta_n k)]dkdvds \tag{1}$$

where g_n is the focused complex-valued pixel in the n-th SAR image, and γ denotes the complex reflectivity. [s, v, k] correspond to elevation, linear velocity, and thermal amplitude, respectively, while [Δs, Δv, Δk] represent the full extent of each parameter. $\xi_n = 2B_{\perp n}/\lambda R$ [m^{-1}] is the spatial (elevation) frequency, where $B_{\perp n}$, λ, and R are the perpendicular baseline, wavelength, and slant range distance, respectively. $\eta_n = 2t_n/\lambda$ [s/m] is the velocity frequency, with t_n being the epoch. $\zeta_n = 2T_n/\lambda$ [K/m] is the thermal frequency, where T_n represents the local temperature.

Discretizing the continuous signal modal (1) along all three directions within their respective extents results in the following form (Ma and Lin 2016)

$$\boldsymbol{g} = \boldsymbol{A}\gamma \tag{2}$$

where

$\boldsymbol{g} = [g_1, \ldots, g_N]^T$ ($(\cdot)^T$ is the transpose operator) is the $N \times 1$ measurement vector for each pixel,

$\boldsymbol{A} = [\boldsymbol{a}(s_1, v_1, k_1), \ldots, \boldsymbol{a}(s_{M_s}, v_{M_v}, k_{M_k})]$ is the $N \times M$ sensing matrix composed of M steering vectors $\boldsymbol{a}$ in the size of $N \times 1$:

$$\boldsymbol{a}(s_p, v_q, k_l) = \begin{bmatrix} exp\left[j2\pi\left(\xi_1 s_p + \eta_1 v_q + \zeta_1 k_l\right)\right] \\ \vdots \\ exp\left[j2\pi\left(\xi_N s_p + \eta_N v_q + \zeta_N k_l\right)\right] \end{bmatrix}$$

$$\forall p = 1, \ldots, M_s$$

$$\forall q = 1, \ldots, M_v$$

$$\forall l = 1, \ldots, M_k \tag{3}$$

and $\gamma = [\gamma(s_1, v_1, k_1), \ldots, \gamma(s_{M_s}, v_{M_v}, k_{M_k})]^T$ is the $M \times 1$ discrete reflectivity vector. The number of discrete samples along the elevation, linear velocity, and thermal amplitude dimensions are M_s, M_v, and M_k, respectively, so $M = M_s \times M_v \times M_k$. The corresponding discrete intervals are $\delta s = \Delta s/(M_s - 1)$, $\delta v = \Delta v/(M_v - 1)$, and $\delta k = \Delta k/(M_k - 1)$.

Inverting (2) gives the spectral estimator $\hat{\gamma}$:

$$\hat{\gamma}(s_p, v_q, k_l) = \frac{\left|\boldsymbol{a}(s_p, v_q, k_l)^H \boldsymbol{g}\right|}{||\boldsymbol{a}(s_p, v_q, k_l)||_2 ||\boldsymbol{g}||_2} \tag{4}$$

where $(\cdot)^H$ denotes the Hermitian operator (transpose and conjugate operation), and $||\cdot||_2$ represents the L2 norm. This spectral estimator is known as beamforming, and the resulting output is the normalized tomographic magnitude (NTM) (Figure 2). If the maximum NTM exceeds a specified threshold, both the start and end PPSCs are classified as true SPSs, and a set of preliminary relative parameters are determined for the end PPSC. Compared to other tomography reconstruction methods, beamforming is efficient and robust (Reigber and Moreira 2000), but it has the drawback of lower resolution due to limited parameter discretization. Another issue is the inclusion of all SAR observations in the beamforming process, which may degrade the precision of parameter estimation if some of the observations have low signal-to-noise ratio (SNR). To address these limitations, the preliminary estimates are refined using a robust M-estimator (Huber 1964). This process begins with temporal phase unwrapping on the end PPSC, after which the unwrapped phase is modeled as a linear combination of the following components:

$$\Delta\varphi_n = 2\pi(\xi_n s' + \eta_n v' + \zeta_n k') \tag{5}$$

where $\Delta\varphi_n$ is the unwrapped phase on the end PPSC at the n-th acquisition epoch. By solving this equation using an iteratively reweighted least squares inversion scheme (the M-estimator) (Ma and Lin 2016), we can obtain a refined set of relative parameter estimates $[\hat{s}', \hat{v}', \hat{k}']$ for the end PPSC. After retrieving the relative parameters for all the arcs, these values are integrated using network adjustment to derive the absolute parameter estimates $[\hat{s}, \hat{v}, \hat{k}]$ using a global reference point for the entire area.

The second-tier network is designed to detect the remaining single PSs (SPSs) and all double PSs (DPSs). First, the SPSs identified in the first-tier network, referred to as reference SPSs, are removed from the SAR images. Secondary PS candidates (SPSCs) are then selected based on pure amplitude thresholding, due to their lower temporal stability in reflectivity. Each SPSC is connected to the nearest reference SPS, forming local star networks and eventually the entire second-tier network. Using the same process of beamforming, temporal unwrapping, relative parameter estimation, and network adjustment, the absolute parameters of qualified SPSs are estimated.

Double PSs (DPSs) are identified using the local maximum ratio method. This ratio is calculated between the two largest local maxima in the NTM spectrum. If the ratio exceeds a specified threshold, the pixel is considered to contain DPS, and the corresponding parameters are estimated following the same flow for SPSCs.

2.2. Extraction of short-wavelength (detrended) signals

The LOS velocities obtained from Tomo-PSInSAR contain both long- and short-wavelength signals. The long-wavelength ground deformation primarily arises from tectonic movements and ground subsidence due to groundwater extraction. In contrast, deformation associated with man-made structures is predominantly short-wavelength, typically spanning tens to hundreds of meters. To eliminate long-wavelength signals, a common approach is to fit the velocity field with a bilinear or biquadratic polynomial function, which can also account for residual long-wavelength errors caused by imprecise orbit, tropospheric, or ionospheric noise (Simons and Rosen 2015). This approach, however, may not align with our goals, as previous InSAR studies of the Taipei Basin have revealed ground deformation patterns of intermediate wavelengths, usually a few kilometers in scale, with local variations potentially linked to geological heterogeneity and groundwater extraction history (Lin 2022; Tung et al. 2016). To better address these ground-related signals, we devise the following procedure to estimate and remove the long-wavelength signals.

We first divide the study area into 0.05°× 0.05° (about 5 km × 5 km) tiles and extend each tile by an additional 0.005° on all sides to create 0.01° overlapping regions with neighboring tiles. A third-order bilinear polynomial surface is fitted to the LOS displacement velocity on a tile-by-tile basis. These fitted surfaces are mosaicked together using a linearly weighted sum of neighboring tiles within the overlapping regions. Finally, the composite long-wavelength signal mosaic is subtracted from the LOS velocities to isolate the desired short-wavelength (detrended) signals. The 0.05° tile size is chosen based on the following two criteria: the resulting mosaicked long-wavelength velocity field should look smooth, and the detrended velocity field should have zero mean and unskewed probability distribution (see insets in Figure 6(c,d}). If the tile size is not appropriate, wide-area residual would appear; if the mosaicking process is flawed, zonal artifacts would occur. This detrending process may potentially introduce a minor velocity ramp to the data in some places, but it should not affect the subsequent SHM analysis significantly due to the gentle nature of the third-order polynomial over a 5 km × 5 km area.

2.3. Estimation of building settlement and tilt

To perform SAR-based SHM, we first determine the building to which each scatterer is associated. For this purpose, we utilize building footprints from the OpenStreetMap (OSM) Geofabrik repository, specifically for the Taiwan region (http://download.geofabrik.de/asia/taiwan.html, last accessed in June 2024). After mapping scatterers to the corresponding building polygons, we proceed to analyze two types of deformation: building settlement and tilt (see workflow in Figure 3).

The information used for the analysis is the scatterer's linear velocity. The original Tomo-PSInSAR velocity values are in the LOS direction, representing a combination of both horizontal (primarily east-west) and vertical motions. Positive velocities indicate motion toward the satellite, which can correspond to either eastward or upward displacement, while negative velocities indicate motion away from the satellite, signifying either westward or downward displacement.

Building deformation, particularly tilt, involves both horizontal and vertical displacements. However, building tilt values are usually very small, mostly less than 1/1000, with values exceeding 1/40

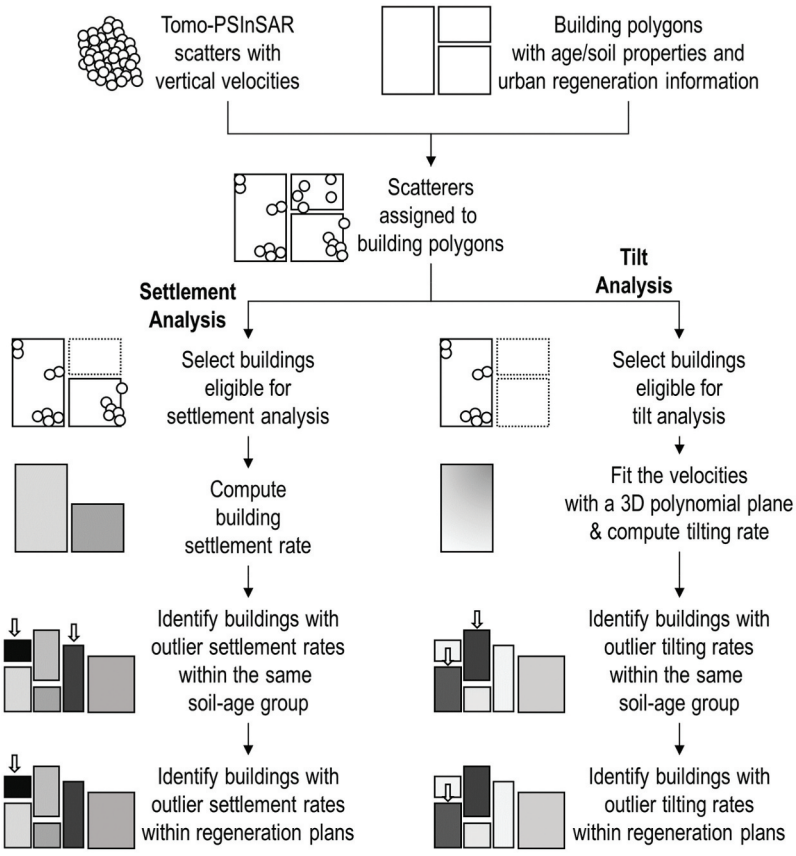

Figure 3. Flowchart of building settlement and tilt estimation.

indicating the need for demolition (Table 2) (Charles and Skinner 2004; Tu et al. 2011). In this regard, building tilting rates should also encompass horizontal components 40–1000 times smaller than the vertical components. Therefore, we assume that the short-wavelength signals are dominated by vertical displacement and apply the following equation to convert the velocities from the LOS direction to vertical:

$$V_Z = \frac{V_{LOS}}{\cos(\theta)} \tag{6}$$

Equation (6) is a simplified form of equation (5.1.1) in Hanssen (2001). It assumes that horizontal velocities (mainly the east component) have minimal contribution to V_{LOS}. In reality, it is possible that localized horizontal displacements, such as those near a pumping well (Burbey 2006), may exist in V_{LOS} and be converted into V_Z. Such ambiguity, however, should be limited in amplitude, given that groundwater extraction has been prohibited since the early 1970s (Chen et al. 2007). Hence, any remnant, localized horizontal displacement caused by hydrodynamic lag effect (a delay in the propagation of fluid-pressure changes between the aquifers and aquitards) should have decayed with time (Galloway, Jones, and Ingebritsen 1999). Another potential source of error arises from buildings undergoing permanent volumetric changes, such as concrete dilation and fractures, in which case the corresponding horizontal displacement might also be projected into V_Z.

To ensure a more conservative and consistent analysis, we select only buildings with at least six scatterers ($n_s \geq 6$) for SHM analysis (Table 1). This threshold is determined through a series of tests with $n_s \geq 4$, 6, 8, and 10. The tests reveal that at larger n_s values (6, 8, and 10), the number of eligible buildings decreases, while the number of resolvable deformation anomalies remains mostly similar. When n_s is reduced to 4, the number of eligible buildings increases, but more unreliable (and large) anomalies occur due to a smaller number of points used in the SHM analysis. The value of $n_s \geq 6$ is therefore selected. This value should be reassessed when applying the SHM analysis approach to a different dataset.

To identify buildings suitable for vertical settlement analysis, we set the following criteria. First, the

Table 1. Criteria for buildings eligible for vertical settlement and titling analysis.

	Vertical Settlement	Tilting
Number of scatterers n_s	≥6	
$\sigma_{\bar{V}_Z^{bldg}}$ [mm/yr]	$<[\bar{\varepsilon}_V - \sigma_{\varepsilon_V}]$ (<1.3)*	–
Negative velocity constraint	$\left[\bar{V}_Z^{bldg} + \sigma_{\bar{V}_Z^{bldg}}\right] < 0$	$\bar{V}_Z^{bldg} < 0$
Spatial coverage of scatterers in X [% of building X dimension]	≥33	≥50
Spatial coverage of scatterers in Y [% of building Y dimension]	≥33	≥50
V_Z RMSE in 3D plane fitting [mm/yr]	–	$<\bar{\varepsilon}_V$ (<1.8)*

$\bar{V}_Z^{bldg}$: mean V_Z of all scatterers within the building block [mm/yr]
$\sigma_{\bar{V}_Z^{bldg}}$: standard deviation of all scatterer V_Z within the building block [mm/yr]
$\bar{\varepsilon}_V$: mean V_Z uncertainty of the entire MTInSAR dataset [mm/yr]. Refer to inset in Figure 6e
σ_{ε_V}: standard deviation of V_Z uncertainties [mm/yr]. Refer to inset in Figure 6e
All values are converted from LOS to vertical using eq (6)
*The values used in this study

standard deviation of V_Z among the points within a building polygon ($\sigma_{\bar{V}_Z^{bldg}}$) must be less than one standard deviation below the mean velocity uncertainty of the entire MTInSAR dataset ($\bar{\varepsilon}_V$), which gives a threshold of approximately 1.3 mm/yr in this case (~1.1 mm/yr in LOS, or 1.3 mm/yr in vertical direction; Table 5). This criterion ensures the robustness of homogeneous settlement. Second, we apply a conservative negative velocity constraint, requiring that the building block's mean $\bar{V}_Z^{bldg}$ plus one standard deviation $\sigma_{\bar{V}_Z^{bldg}}$ remains less than zero. This criterion ensures the exclusion of blocks with predominantly positive V_Z values. Third, we observe that in some cases, the scatterers may originate from only one corner of the building. To ensure that the analysis accurately represents the uniform settlement of the entire building, we limit the analysis to buildings where the scatterer distribution spans at least 33% of the X and Y dimensions of the building (Table 1). Sensitivity tests using scatterer spatial coverage criteria ranging from 10% to 90% indicate that the number of eligible buildings declines linearly with increasing thresholds, while the fraction of outliers (buildings with anomalous settlement) remains stable up to 33% but decreases linearly beyond this point. Based on these trends, 33% may represent a balance between retaining a sufficient number of eligible buildings for analysis and minimizing outliers from scatterers with limited spatial coverage. We therefore set 33% as the criterion for settlement analysis.

We then calculate the mean V_Z for each building ($\bar{V}_Z^{bldg}$). To assess how factors such as soil properties and building ages influence building deformation, we further categorize the buildings by using soil properties (such as the SPT-N values, see section 4.4) and then by building ages. Within each soil-age group, we apply the following criterion to identify buildings with outlier settlement rates:

$$\bar{V}_Z^{bldg} < V_{z,Q1}^{grp} - 1.5 * \left(V_{z,Q3}^{grp} - V_{z,Q1}^{grp}\right) \tag{7}$$

where $V_{z,Q1}^{grp}$ and $V_{z,Q3}^{grp}$ represent the first and third quartiles of the velocities within each group.

For tilt analysis, we fit the scatterer V_Z values within each building block using the following equation:

$$V_Z = c_1 + c_2X + c_3Y + c_4Z \tag{8}$$

X and Y are the local Cartesian coordinates of the scatterers, while Z is represented by the elevation parameter (s) obtained through Tomo-PSInSAR processing (Equations 1–5). The first three terms of the equation describe a 3D plane, and the last term accounts for any covariance between V_Z and Z. The underlying assumption is that building tilt behaves like a rigid block rotation along a horizontal axis, meaning that V_Z depends on mainly X and Y. Any significant dependence of V_Z on Z, as observed in some cases, is attributed to the tradeoff effect during the parameter estimation in (5).

Table 2. Required actions in Taiwan at different building tilt values (Tu et al. 2011) and long-term outcomes at different tile rates.

Tilt	Required Action	Tilt Rate [yr^{-1}]	Long-term outcomes if the condition lasts
<1/200	Restoration (possible)	1/4000	Restoration in 20 years Reconstruction in 100 years
1/200–1/40	Restoration and reinforcement	1/2000	Restoration in 10 years Reconstruction in 50 years
>1/40	Demolition and reconstruction	1/1000	Restoration needed in 5 years Reconstruction in 25 years

In the tilt analysis, as the scatterers' velocities change within the same building polygon, we do not set any criterion based on the velocity standard deviation. Compared to settlement analysis, we apply a less conservative negative velocity constraint, requiring the building block's mean velocity $\bar{V}_Z^{bldg}$ to be less than zero (Table 1). This criterion allows some positive V_Z values to account for instances where parts of the building may tilt upward during tilting. As tilt detection is more sensitive to the even distribution of scatterers than settlement detection, a higher criterion for scatterer distribution is likely needed. Sensitivity tests again indicate that while the number of eligible buildings declines linearly with increasing thresholds, the fraction of tilt outliers remains stable up to 50% but decreases linearly beyond this point. We therefore set 50% as the criterion for tilt analysis. After screening buildings with this criterion, we further narrow down the tilt analysis eligibility using the following index: the root mean square error (RMSE) between the observed and fitted V_Z values. Buildings with RMSE greater than the mean velocity uncertainty of the entire MTInSAR dataset $\bar{\varepsilon}_V$ (1.5 mm/yr in the LOS direction, or 1.8 mm/yr in the vertical direction; Table 5) are deemed to be of poor quality and are excluded from the analysis.

After fitting the building scatterer V_Z using (8), we can compute the tangent of the angle between the plane normal vector $n_p = [-c_2, -c_3, 1]$ and the vertical unit vector $n_z = [0, 0, 1]$. This is done by combining the vector cross-product equation ($|n_p \times n_z| = |n_p| n_z \sin\theta$) and dot-product equation ($n_p \cdot n_z = |n_p| n_z \cos\theta$) into the following:

$$\dot{\alpha} = \frac{|n_p \times n_z|}{n_p \cdot n_z} \tag{9}$$

where $\dot{\alpha}$ is the tilting rate, expressed in units of yr^{-1}, indicating the rate of change in tilt per year. A tilting rate of 1/1000 indicates an increase of 1-m vertical difference per 1000 m of horizontal distance per year. After calculating the tilting rate for all buildings, we again categorize them into different soil-age groups and apply the following criterion to identify buildings with outlier tilting rates:

$$\dot{\alpha}^{bldg} > \dot{\alpha}_{Q1}^{grp} + 1.5 * \left(\dot{\alpha}_{Q3}^{grp} - \dot{\alpha}_{Q1}^{grp}\right) \tag{10}$$

where $\dot{\alpha}_{Q1}^{grp}$ and $\dot{\alpha}_{Q3}^{grp}$ represent the first and third quartiles of the tilting rate within each group.

3. Study area: Taipei Basin

The Taipei Basin is a half-graben formed during post-orogenic extension in northern Taiwan since 0.8 Ma (Teng et al. 2001). The reactivation of a former reverse fault into the Shanchiao fault caused the asymmetric subsidence of the Tertiary basement and subsequent deposition of Holocene alluvio-lacustrine sediments (Figure 4a). The topmost layer, the Holocene Sungshan formation (formed ~12 Ka), consists of alternating sand, silt, and muddy clay, reflecting environmental variations driven by changes in sea level. These sediment layers generally thicken northwestward toward the Shanchiao fault, reaching a maximum thickness of ~120 m just east of the fault. Conversely, toward the southeastern side of the basin, the layers gradually thin and taper off, with the Pleistocene or even Miocene basement reaching the surface (Lee et al. 2011; Wang et al. 2004). Within the top 30 m – a depth range for most construction activities – estuarine muddy clay transitions upward into fluvial sand and floodplain mud, deposited during the most recent sea-level regression (Chen et al. 2008). The muddy clay in this depth range exhibits low mechanical strength, with a water content close to its liquid limit of 30% (Lee et al. 2011; Wang et al. 2004). In terms of structural activities, borehole records indicate active extension during the early-mid Holocene, with episodic displacements of 2.3 to 4.5 m along the fault, potentially causing earthquakes of magnitude 6.9 to 7.1 (Huang et al. 2007). Although these events may have a long recurrence interval of ~5,000 years, other large earthquakes in Taiwan, like the Mw 7.6 Chi-Chi earthquake in 1999 and the Mw. 7.3 Hualien earthquake in 2024, have also caused building damage in the basin due to site amplification effects from the soft sediments and the half-graben basin structure (Chan et al. 2020; Cheng et al. 2010; Fletcher and Wen 2005).

In addition to active faults, the Tatun Volcano, located on the northern edge of the Taipei Basin, poses potential threats (Figure 4a). The volcano's last magmatic eruption occurred around 20 Ka, with a possible effusive eruption around 6 Ka (Belousov et al. 2010; Chen and Lin 2002). Recent seismic activities suggest ongoing volcanic processes, with several phreatic eruptions in the past decade (Lin 2017; Pu et al. 2020). The associated seismic hazards within the basin should not be underestimated

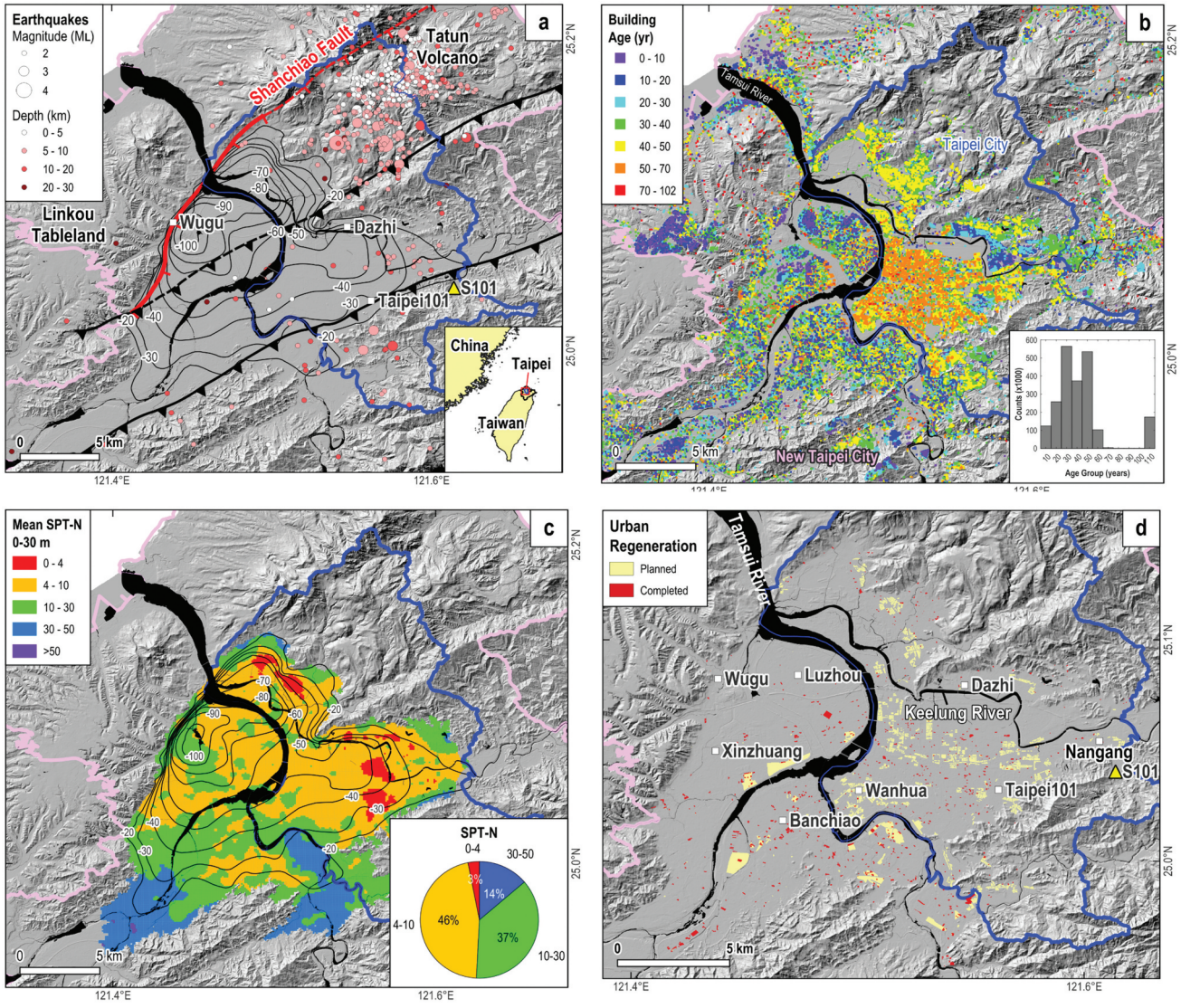

Figure 4. Geology, building age, soil types, and urban regeneration plans of the Taipei Basin. (a) Geological features and earthquake records around the Taipei Basin. The black contour lines indicate the depth (in meters) of the Holocene Sungshan formation, the topmost layer in the basin composed of silt and mud (Wang et al. 2004). Among all three faults shown, only the Shanchiao fault is considered seismogenic (Shyu et al. 2020). Earthquake records span from 1991 to 2023 (data source: central weather administration Taiwan geophysical database management system, https://gdms.Cwa.gov.tw, last accessed in June 2024). M_L denotes local magnitude (refer to https://scweb.Cwa.gov.tw/en-us/page/intro/44 for more details; last accessed in April 2024). Blue and pink polygons outline the borders of the Taipei City and the New Taipei City, respectively. S101 marks the continuous GNSS station located on the roof top of institute of earth sciences building. (b) Building ages as of 2022. See section 4 for details about data sources. Inset: histogram of building ages. c. Mean (0–30 m) standard penetration test number (SPT-N) (data source: https://geotech.Gsmma.gov.tw/imoeagis/Home/supply, last accessed in June 2024). Inset: distribution of SPT-N values. d. Planned and completed urban regeneration areas within the Taipei Basin as of 2022. See section 4 for the sources of data.

Besides frequent seismic activities and shaking amplification effects in the basin, high summer temperatures (>30°C from June to September), an annual precipitation rate of ~2,370 mm/yr, and frequent typhoon visits can accelerate the premature deterioration of reinforced concrete structures by promoting chemical reactions (Auld, Klaassen, and Comer 2006; Stewart, Wang, and Nguyen 2012). These reactions lead to steel bar corrosion, causing expansion and fractures in the surrounding concrete and ultimately reducing the bonding strength between the concrete and steel bars (Chiu, Tu, and Zhuang 2016; Lee and Cho 2009). This loss of mechanical strength makes many older structures in the basin increasingly susceptible to deformation under load and vulnerable to failure during large earthquakes. Identifying these at-risk buildings becomes a necessary task for enhancing urban resilience.

4. Data

4.1. Synthetic aperture radar imagery

We use 27 TerraSAR-X (TSX) and 14 TanDEM-X (TDX) HH-polarization stripmap images (41 images in total) for the Tomo-PSInSAR analysis. A standard PSInSAR analysis (Hooper, Segall, and Zebker 2007) with the Shuttle Radar Topography Mission DEM (Farr et al. 2007) is also conducted in parallel using the same dataset for comparison. The images are acquired on a descending path between 8 September 2017 and 1 December 2019 (Figure 5a). The spatial resolution is 1.2 m in the slant range and 3.3 m in the azimuth direction. Table 3 provides a summary of the image specifications. The baseline plot (Figure 5b) shows the distribution of spatial baselines, with a total perpendicular baseline span $\Delta B_{\perp}$, which serves as the aperture in the TomoSAR elevation direction, measuring 775.5 m.

4.2. Global navigation satellite system (GNSS) data

To validate the velocities obtained from SAR data, we use records from nine continuous GNSS ground stations across the Taipei Basin (Figure 5a). These stations are selected based on the overlapping observation time span with the SAR dataset. The daily displacement time series were downloaded from the Taiwan Geodetic Model (TGM) website (https://tgm.earth.sinica.edu.tw/, last accessed in June 2024) and projected to form the LOS displacement time-series for all stations. Since InSAR velocities are relative to a local reference point, we set the GNSS station S101 as a reference for both InSAR and GNSS observations. This station is situated on the rooftop of the Institute of Earth Sciences building in the eastern Taipei Basin, where the soft sediment layer is thin, and mid-Miocene sandstone lies close to the surface (National Geological Data Warehouse, https://geomap.gsmma.gov.tw, last accessed in December 2024) (Figure. 4a). Established on 1 January 1993, the station has operated continuously for over 30 years. The mean LOS displacement velocity at S101 is estimated by fitting the displacement time-series with a linear term for velocity and sinusoidal terms (sines and cosines for the periods of one year and half year) for annual and semiannual variations (Nguyen et al. 2022). The mean LOS displacement velocity from S101 is then subtracted from the displacement time-series for all other GNSS stations.

To compare the InSAR LOS velocities with GNSS LOS velocities, we select an area within a 250-m radius of each GNSS station. The InSAR time-series for all scatterers within this radius are fitted using the same parameterized formula applied to the GNSS time-series. The mean InSAR velocities and standard

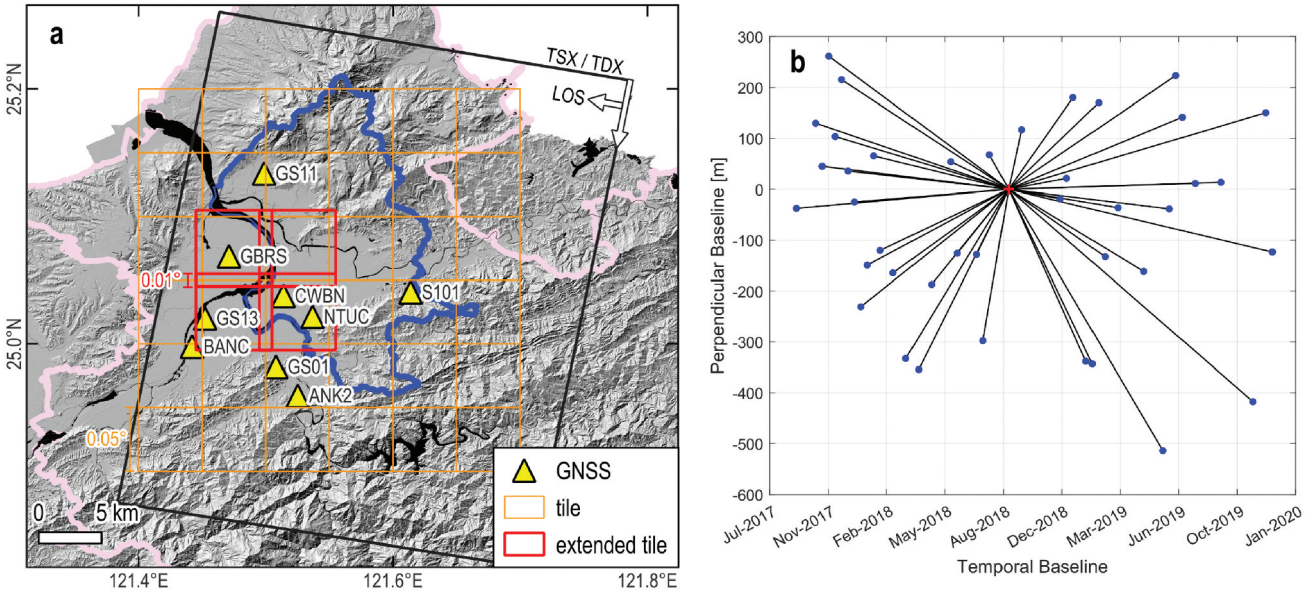

Figure 5. SAR data used in this study. a. Footprint and LOS direction of the TSX and TDX imagery. The red and orange tiles indicate the areas used for the evaluating long-wavelength signals in the LOS velocities. Blue polygon: Taipei City. Pink polygon: new Taipei City. b. Baseline plot of the SAR images. The red cross represents the reference image from September 6, 2018. The total perpendicular baseline span $\Delta B_{\perp}$ is 775.5 m. Black lines represent the processing network for PSInSAR.

Table 3. TerraSAR-X/TanDEM-X image specifications.

Wavelength λ [cm]	3.1
Polarization [-]	HH
Incidence angle θ [deg]	33.2
Number of acquisitions N	41
Observation period [year]	2.23
Slant range between satellite and target R [km]	603.65
Total perpendicular baseline span $\Delta B_{\perp}$ [m]	775.5
Standard deviation of the elevation aperture σ_B [m]	15.3
Max. resolvable elevation Δs [m][*1]	934.0
Slant range resolution ρ_r [m]	1.2
Azimuth resolution ρ_x [m]	3.3
Elevation resolution ρ_s [m] [*2]	12.1
Elevation error $\sigma_{\hat{s}}$ [m], SNR=10 dB[*3]	3.4
Elevation error $\sigma_{\hat{s}}$ [m], SNR=5 dB[*3]	4.8

[*1] $\Delta s \ll (\rho_r R)/\Delta B_{\perp}$ (Zhu and Bamler 2010b); it means the maximum scatterer elevation above a given reference ground that SAR tomography is able to resolve.

[*2] $\rho_s = \lambda R/(2\Delta B_{\perp})$ (Zhu and Bamler 2010b).

[*3] $\sigma_{\hat{s}} = \lambda R/\left(4\pi\sqrt{N}\sqrt{2SNR}\sigma_B\right)$according to Cramér-Rao lower bound (CRLB) (Zhu and Bamler 2010a).

deviations are then calculated based on an ensemble of linear velocities.

4.3. Building age and urban regeneration data

For building ages in Taipei City, the dataset was made available on GitHub (https://github.com/imdataman/taipei-house-age-map, last accessed in June 2024). It is created by comparing the address and age information in the Taipei City building construction license dataset (the latest online database available at https://data.gov.tw/dataset/128204., last accessed in Dec 2024) with the national address system (https://luz.tcd.gov.tw/WEB/default.aspx, last accessed in June 2024) to generate the coordinates for each building. This building age dataset was created in December 2016. To account for the time difference with the SAR images, we added 3 years to all building ages, making it the youngest building age in Taipei City 4 years. For New Taipei City, the building age dataset is provided directly by the Land Administrator Department, New Taipei City Government, with the online version accessible via the i-Land system (https://i.land.ntpc.gov.tw/landsar/landsta/#, last accessed in June 2024). The dataset represents the ages at the end of 2022, so 3 years were subtracted from all building ages to align with the analysis time frame. Buildings with negative ages are then excluded. The overall age distribution of the buildings is shown in the inset of Figure 4b. As both age datasets are point-based (Figure 4b), to attribute age readings to individual buildings, the datasets are spatially overlaid with the OSM building polygons. If multiple points fall within the same polygon, their median value is assigned. Given location errors in both the age datasets and the building polygons, this process may lead to misattribution of points and building age errors.

For the urban regeneration dataset in Taipei City, the latest regeneration plan (2018) is available from the Taipei City Urban Regeneration Office (https://uro.gov.taipei/cp.aspx?n=3C7DB2F1081E962B, last accessed in June 2024). Completed areas are digitized directly from the Taipei City Urban Development Review Map (https://bim.udd.gov.taipei/UDDPlanMap, last accessed in June 2024) for cases completed between 2001 and 2022. For New Taipei City, both the planned and completed areas are digitized from the New Taipei City Government Urban and Rural Information Inquiry Platform (https://urban.planning.ntpc.gov.tw/NtpcURInfo/map.aspx, last accessed in June 2024) for the period between 2002 and 2022. The combined map is shown in Figure 4d. When evaluating the efficacy of applying SAR-based SHM for urban regeneration (section 5.4), buildings labeled as completed within the planned areas are excluded from the analysis. Due to the difference in time frame, buildings rebuilt between the last SAR acquisition (October 2019) and the end of the urban regeneration dataset (2022) will be omitted from the analysis, causing potential undercounts.

4.4. Soil properties

More than 1,970 engineering wells were drilled within the Taipei Basin between 1992 and 2013 (Central Geological Survey 2020). According to Ministry of Interior regulations, N-values of standard penetration tests were obtained for the uppermost 30-m soil layer at 1.5-m depth intervals, following the guidelines of the Japanese Road Association (Japanese Road Association 1996). These N-values were then interpolated into grids with a resolution of $100 \times 100 \times 1$ m down to a depth of 30 m. Figure 4c shows the mean N-values between 0 and 30 m (referred to as SPT-N in this study). This mean value is used to represent overall soil conditions: SPT-N ≤ 4 for very loose soil, 4–10 for loose soil, 10–30 for medium soil, 30–50 for dense soil, and >50 for very dense soil (Terzaghi, Peck, and Mesri 1996). For our subsequent analysis, we will further categorize the soil into two major types: SPT-

N ≤ 10 for very loose to loose soil, and SPT-N > 10 for medium to very dense soil.

5. Results and discussions

5.1. Comparison of LOS velocities between different InSAR methods

The LOS velocities obtained from Tomo-PSInSAR and PSInSAR are shown in Figure 6a & b. Table 4 provides the statistical comparison between the two methods. Tomo-PSInSAR extracts more than 3.2 million scatterers, about doubling the 1.5 million points extracted by PSInSAR. This difference results in a higher point density for Tomo-PSInSAR (12,218 points/km^2) compared to PSInsAR (5,835 points/km^2). Both methods reveal a similar pattern, indicating that the Taipei Basin is experiencing asymmetric subsidence, with the western part subsiding at higher rates. This pattern is likely due to a combination of interseismic deformation related to the active Shanchiao fault (C.-T. Chen et al. 2007) and ground subsidence caused by both elastic and anelastic ground deformation associated with groundwater changes (Wu et al. 2024). However, the Tomo-PSInSAR results show more negative velocities, with values reaching as low as −28.96 mm/yr compared to −9.89 mm/yr for PSInSAR (Figure 6a & b) (Table 4). This difference may be due to the removal of spatially correlated phases, particularly the long-wavelength residual phase from satellite orbit inaccuracies, in the PSInSAR processing using a spatial-temporal filter (Hooper, Segall, and Zebker 2007). The velocity values and patterns derived from PSInSAR in this study are comparable to those obtained using PSInSAR on Sentinel-1 SAR images over similar periods (Lin 2022). On the other hand, as orbital errors are not accounted for in Tomo-PSInSAR processing, the accuracy of long-wavelength signals may require further improvement, such as by incorporating a spatial-temporal filtering approach during the processing.

The detrended velocity fields reveal differences at local scales (Figure 6c-d). The Tomo-PSInSAR velocity map shows small patches with distinct negative LOS displacement velocity anomalies, with values as low as −18.22 mm/yr, while the PSInSAR result displays a smoother velocity field, with negative velocities limited to −5.99 mm/yr (Table 4). A close-up view of these anomalies (Figure 7) shows that Tomo-PSInSAR points are better aligned with the outline of manmade structures, whereas PSInSAR points are scattered. Additionally, Tomo-PSInSAR points show larger velocity anomalies clustered around specific buildings, while PSInSAR points display little to no anomalies. The better alignment of Tomo-PSInSAR points with building edges and the clustering of anomalies around certain buildings suggest that Tomo-PSInSAR is more effective in providing realistic estimates of building deformation.

In terms of the uncertainties, both methods exhibit increasing velocity standard deviations toward the west (Figure 6e & f). Tomo-PSInSAR generally shows larger uncertainties, with a mean V_{LOS} standard deviation of 1.52 mm/yr compared to 1.43 mm/yr for PSInSAR (Table 4). When validating against GNSS displacement time-series, the original (undetrended) InSAR LOS displacement time series from both methods are comparable, with slightly larger variations than the GNSS time-series due to residual APS effects (Figure 8). The root mean square difference (RMSD) and mean absolute error (MAE) between the Tomo-PSInSAR V_{LOS} and GNSS V_{LOS} are 1.73 and 1.39 mm/yr, respectively, with a mean standard deviation of 1.13 mm/yr across all GNSS stations. For PSInSAR, the RMSD, MAE, and standard deviation are 1.99, 1.38, and 0.96 mm/yr, respectively (Table 4).

Given the large number of scatterers retrieved, the precision in their 3D positions, and comparable uncertainty levels with PSInSAR, Tomo-PSInSAR appears to be a suitable tool for studying deformation at the building level. However, the method has several limitations. First, it has strict requirements regarding the spatial baseline distribution (Table 3). The total baseline span must be sufficiently large, and the baselines of individual passes should be relatively evenly distributed within this range to ensure high-quality tomographic results. Many repeat-pass SAR satellites with global coverages, such as Sentinel-1, have narrow orbital tubes or uneven baseline distributions, which do not meet these requirements. Second, the slant-range resolution needs to be fine enough to allow the retrieval of a greater number of scatterers. At coarse spatial resolution, even if the threshold for the normalized tomographic magnitude is lowered to resolve more scatterers within a single pixel, the number of retrieved scatterers remains significantly lower compared to those obtained from high or ultra-high resolution SAR images. These two limitations largely restrict tomographic applications to high-

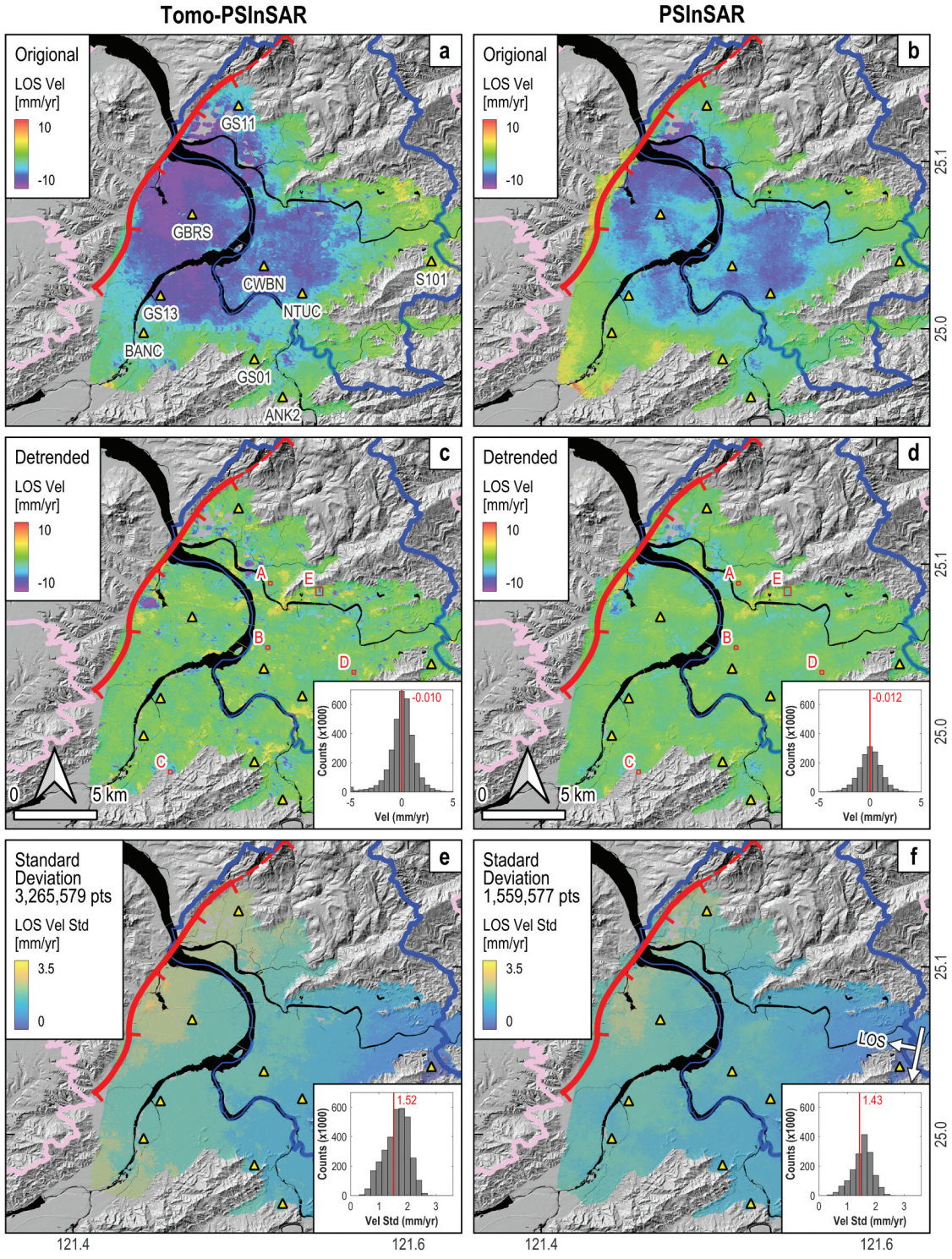

Figure 6. Comparison between tomo-PSInSAR and PSInSAR results.a-b. Original LOS velocities relative to GNSS station S101. c-d. Detrended LOS velocities (with long-wavelength signals removed). See Figure 8 for zoomed-in views of location a to d and and Figure 13 for tilt validation at location e. Inset: distribution of detrended LOS velocities. e-f. LOS displacement velocity standard deviation. The thick red line marks the active Shanchiao fault, with thin ticks indicating the down-thrown side of the crustal block (hanging wall). Inset: distribution of LOS displacement velocity standard deviation. Red line indicates the mean value. Blue polygon: Taipei City. Pink polygon: new Taipei City.

Table 4. Comparison between Tomo-PSInSAR and PSInSAR results.

	Tomo-PSInSAR	PSInSAR
Number of points extracted	3,265,579	1,559,577
Point density [pt/km^2]	12,218	5835
Lower-tail V_{LOS}, original velocity field [mm/yr]*	−29.96	−9.89
Lower-tail V_{LOS}, detrended velocity field [mm/yr]*	−18.22	−5.99
V_{LOS} uncertainties [mm/yr]	1.52±0.42	1.43±0.35
RMSD between original V_{LOS} and GNSS V_{LOS} [mm/yr]	1.73	1.99
MAE between original V_{LOS} and GNSS V_{LOS} [mm/yr]	1.39	1.38
Mean V_{LOS} standard deviation at GNSS sites [mm/yr]	1.13	0.96

*To avoid reporting outliers, the value is read from the 0.01% quantile of the entire dataset.

performance X-band SAR satellites. These satellites, unless specifically tasked, usually focus image acquisitions on large cities outside their home countries, further limiting the geographical applicability of Tomo-PSInSAR.

Finally, as discussed earlier, long-wavelength errors possibly caused by orbital uncertainties exist in the current Tomo-PSInSAR results. Efforts such as incorporating orbital error estimation (Chen, Peng, and Yang 2017; Zhang et al. 2014) in the Tomo-PSInSAR network adjustment (Figure 2), or conducting orbital error isolation by using multispectral wavelet analysis or independent component analysis (Hu et al. 2022) during the post-processing stage will further improve the robustness of the Tomo-PSInSAR results.

5.2. SAR-based SHM in Taipei basin

Based on the criteria set for building SHM analysis (Table 1), a total of 9,816 buildings are eligible for the analysis, representing 11.6% of all building polygons (Table 5). When separating them by soil types (SPT-N ≤ 10 and SPT-N > 10), although the number of buildings in the two groups is different by only 11.4% (51.7% vs. 40.3%), the number of eligible buildings is different by 44% (72% vs. 28%) (Table 5; Figure 9). Such a bias in proportion is also seen in the settlement and tilt analysis, respectively. We will discuss possible explanations of this bias in Section 5.4. Of all eligible buildings, only 56% (5,491) contain age information. The following analysis is conducted on buildings with both SPT-N values and building ages.

For settlement analysis, the buildings are grouped by 2 soil types and 14 age groups between 4 and 110 years. Younger buildings (within 20 years) are grouped in approximately 5-year intervals, as building load tends to induce greater soil consolidation and more variable ground deformation during this period (Ciampalini et al. 2019; van der Horst et al. 2018). Beyond age 20, buildings are grouped evenly in 10-year intervals up to 110 years. In both soil types, the box plot shows that the younger age groups (4 and 6 years) exhibit higher settlement rates and greater variation compared to older age groups. This pattern

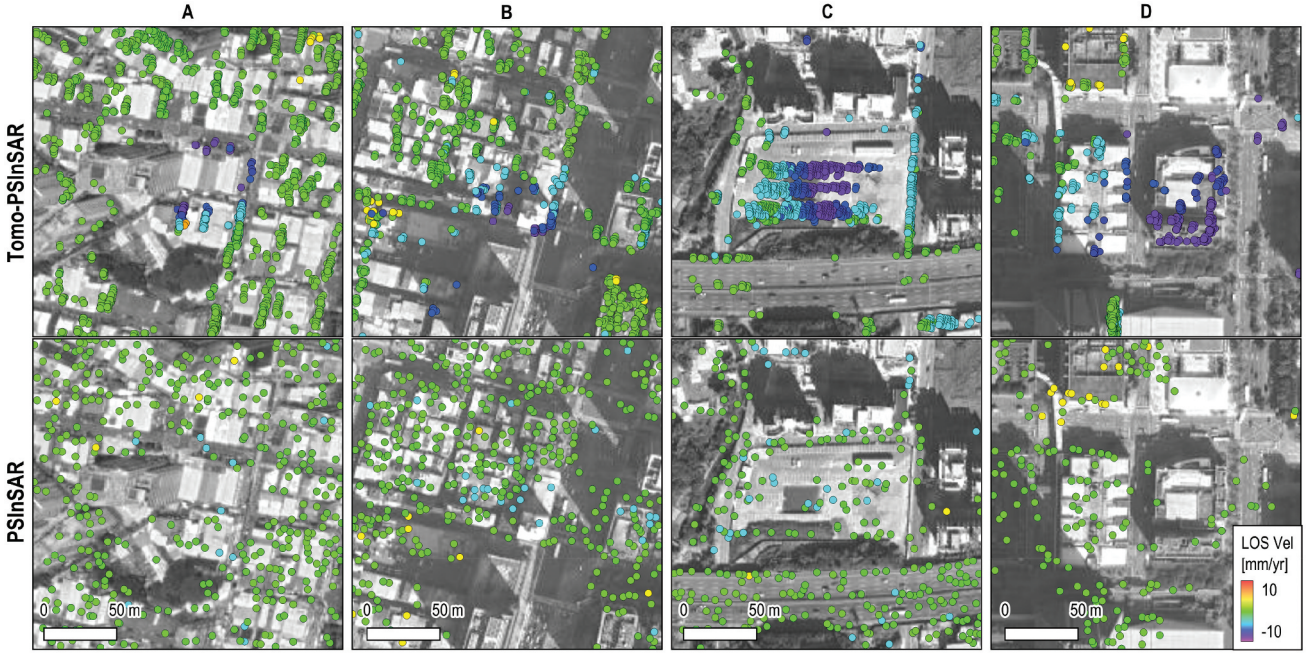

Figure 7. Close-up comparison of tomo-PSInSAR and PSInSAR detrended velocities at selected sites (see Figure 6c for location). Background image source: Google earth. Imagery date: August 31, 2019.

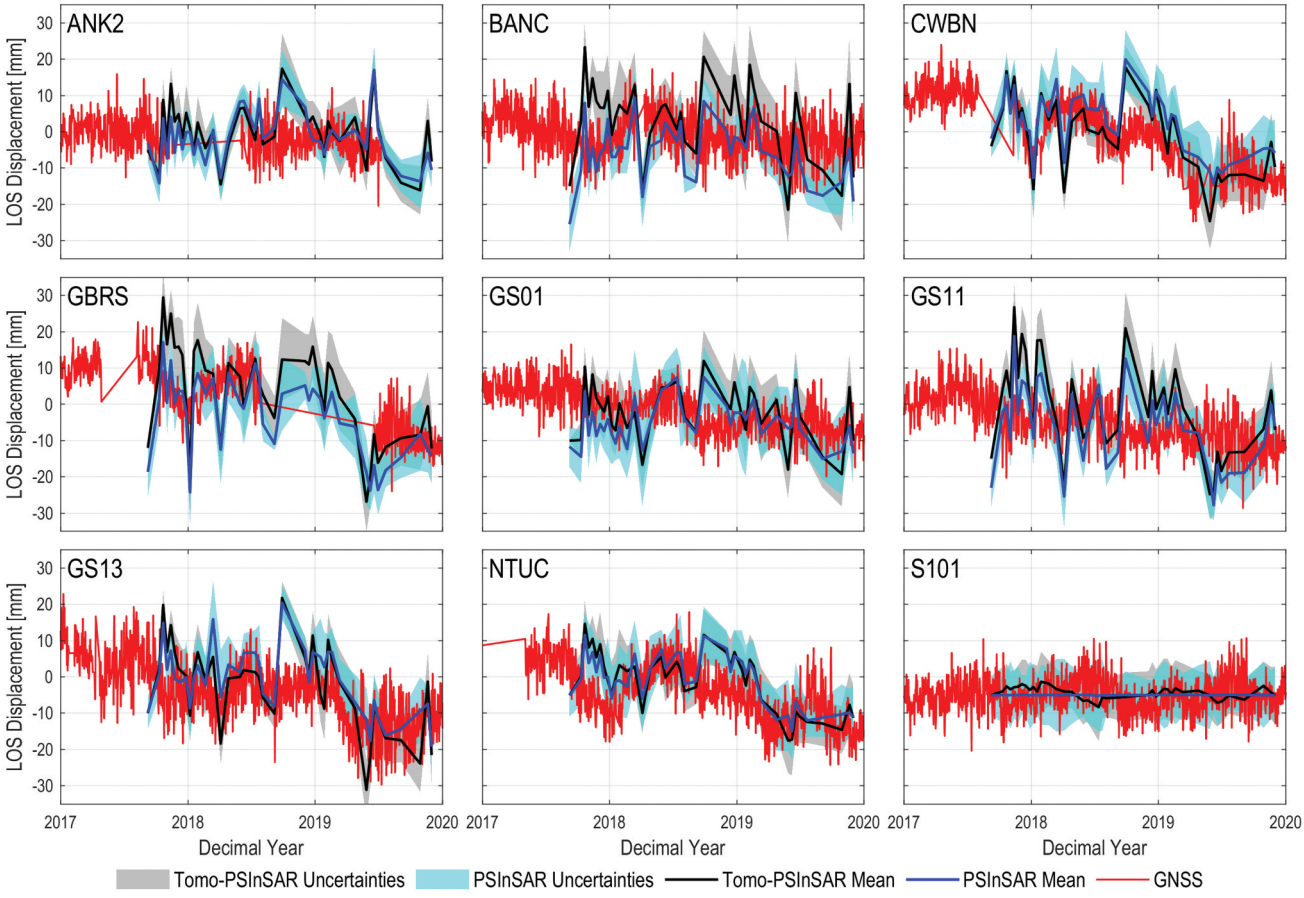

Figure 8. LOS displacement time-series from tomo-PSInsAR, PSInSAR, and GNSS measurements. All time-series are re-referenced (flattened) using the linear velocity obtained at GNSS station S101. Both InSAR time series are presented without detrending.

Table 5. Statistics for building settlement and tilt analysis.

	Settlement	Tilt	Together
(A) Number of all building polygons		84,759	
(A1) SPT-N≤10 [A1/A]		43801 [51.7%]	
(A2) SPT-N>10 [A2/A]		34140 [40.3%]	
(A3) No SPT-N value		6818 [8.0%]	
(B) Number of eligible buildings for analysis* [B/A]	7,474 [8.8%]	6,601 [7.8%]	9,816 [11.6%]
(B1) SPT-N≤10 [B1/B]	5,340 [71.4%]	5,186 [78.6%]	7,064 [72.0%]
(B2) SPT-N>10 [B2/B]	2,134 [28.6%]	1,415 [21.4%]	2,752 [28.0%]
(C) Number of eligible buildings with age information [C/B]	4,199 [56.2%]	3,638 [55.1%]	5,491 [55.9%]
(C1) SPT-N≤10 [C1/C]	3,117 [74.2%]	3,048 [83.8%]	
(C2) SPT-N>10 [C2/C]	1,082 [25.8%]	590 [16.2%]	
(D) Number of outliers according to statistics in each age group	256	279	517 (1,058)†
(D1) SPT-N≤10 [D1/D]	185 [72.3%]	236 [84.6%]	
(D2) SPT-N>10 [D2/D]	71 [27.7%]	43 [15.4%]	
(E) Outlier fraction (D)/(C)	6.1%	7.7%	9.4% (10.8%)†
(E1) SPT-N≤10 (D1)/(C1)	5.9%	7.7%	
(E2) SPT-N>10 (D2)/(C2)	6.6%	7.3%	

*Using criteria set in Table 1. Buildings in areas without SPT-N values are excluded.
†Values in parentheses indicate data after including buildings without age information. Outliers are identified based on the mean and standard deviation value of all samples.

reflects soil compaction due to the loading effects of newly constructed buildings (Figure 10a and 10c). Except for certain soil-age groups with limited building samples (e.g. age group 80 in SPT-N ≤ 10), the mean settlement rates generally decrease with building age (blue boxes in Figure 10a & c). This

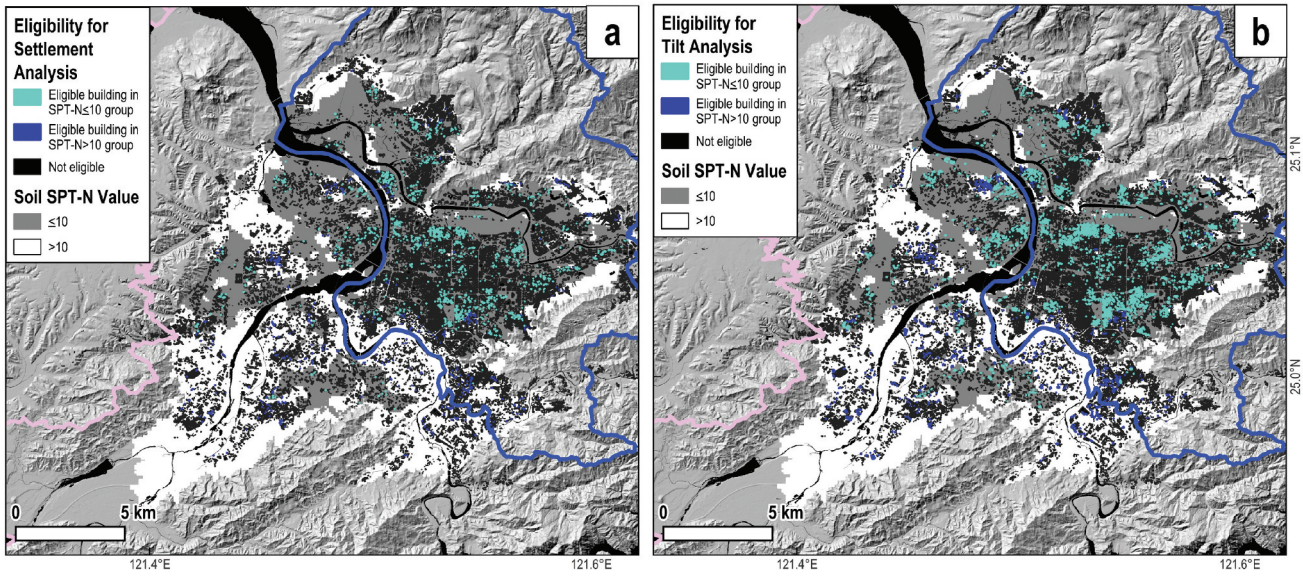

Figure 9. Distribution of buildings eligible for (a) settlement and (b) tilt analysis, categorized by soil types. Blue polygon: Taipei City. Pink polygon: new Taipei City.

trend aligns with the stabilization of soil compaction observed in other cities (van der Horst et al. 2018; Yang et al. 2018). The number of outliers (defined in Equation (7)) is 185 in the SPT-N ≤ 10 group and 71 in the SPT-N > 10 group, accounting for 5.9% and 6.6% of buildings in these groups, respectively (Table 5).

When we further break down the outlier fractions by age groups (Figure 10b & d), a slight increasing trend is observed up to age group 60. Excluding the high outlier fraction in age group 110 within the SPT-N > 10 group, which is likely due to its limited sample size, the highest outlier fraction appears in age group 40 for both soil types. Cases with large settlement rates, peaking at around −14 mm/yr, mostly occur in the age groups of 40 and 50. We perform a series of multivariable linear regression analyses on settlement rates, using age and SPT-N values as predictor variables. The results indicate that for all eligible buildings, the settlement rate decreases at a significant level with increasing age and SPT-N values, possibly reflecting the general soil consolidation trend (model A, Table 6). However, when analyzing only outlier settlement rates, neither the model nor the individual variables reach statistical significance (model B). Further examination of outlier fractions and maximum outlier rates by groups among buildings aged less than 50 years (where more samples are concentrated) reveals that large outlier settlement rates, represented by the 90th quantile in each age-SPT-N group, increase with building age at a significant level (model D), different from the general soil consolidation trend. Meanwhile, outlier fractions also increase slightly with age (model C). The SPT-N values do not emerge as significant predictors in outlier-related regression models, even when we categorized into smaller interval groups. These findings suggest that older buildings may exhibit higher outlier fractions and greater anomalous settlement, but the overall outlier settlement rates are likely influenced by additional unmodeled factors, such as building materials, foundation types, and micro-topography or geology.

Figure 10e & 10f present an example of a building with a settlement rate of -7.3 ± 0.2 mm/yr. The tilting rate of this building, 1/23,837 per year, is well below the average of 1/13,983 per year for the SPT-N≤10 group, indicating that the building is experiencing relatively uniform sinking.

For building tilt analysis, a total of 6,601 buildings (7.8% of the OSM building polygons) meet the criteria in Table 1, among which only 3,638 buildings contain both age and soil property information. Compared to vertical settlement, which has an overall outlier fraction of 6.1%, tilting demonstrates a slightly higher fraction of 7.7% (Table 5). Given the larger number of samples in the SPT-N ≤ 10 group (3,048), there are also more outliers (236), compared to 590 samples and 43 outliers in the SPT-N > 10 level. Proportionally, both soil types have a similar fraction of outliers (7.7% vs. 7.3%). When further breaking down by age groups, age groups 6 to 60 in SPT-N ≤ 10 have outlier fractions between 8% and

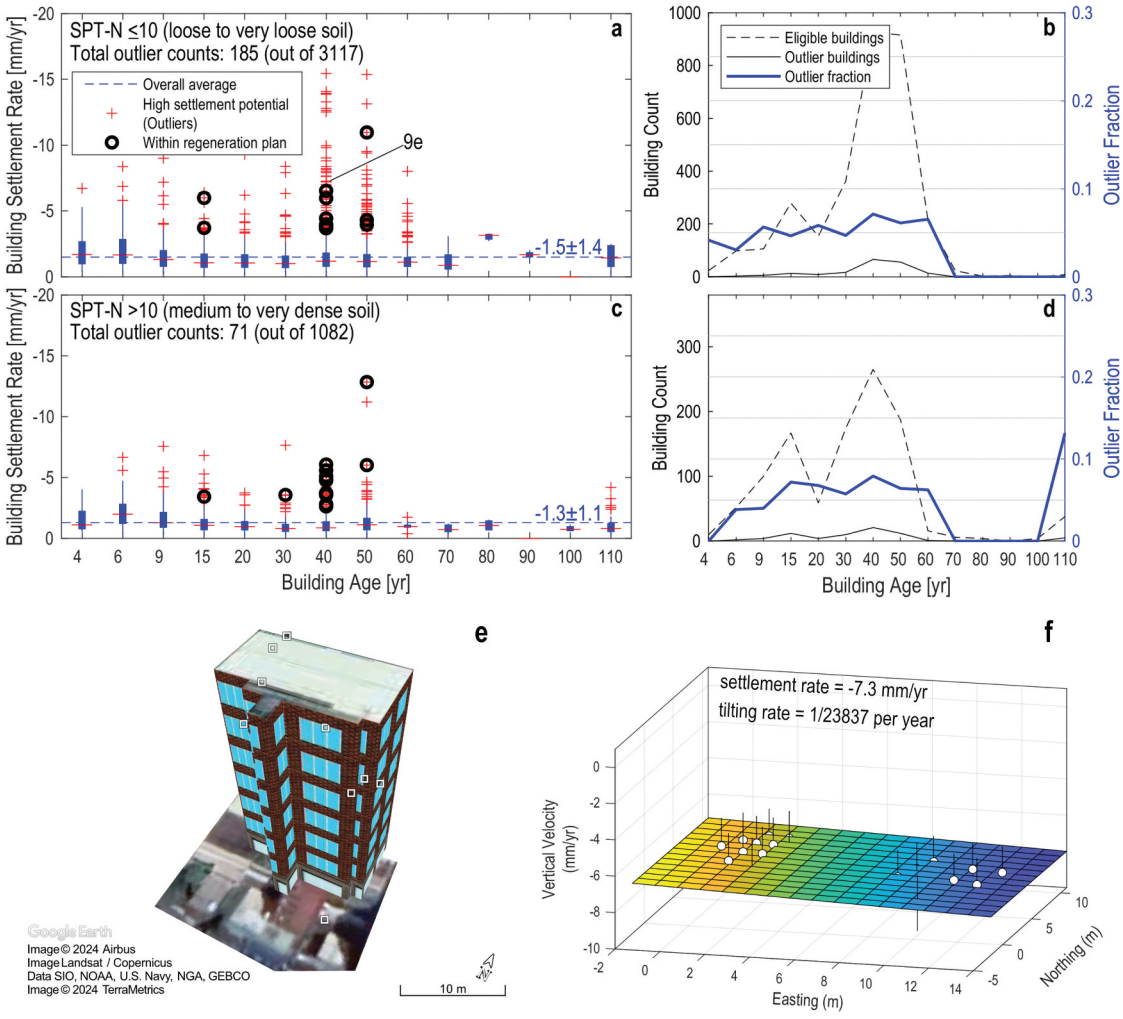

Figure 10. Boxplot statistics and example of building settlement rates across different soil-age groups. a-b. Statistics of building settlement rates and building counts for soils with SPT-N≤10. Outliers are defined based on Equation (7). c-d. Statistics for buildings on soils with SPT-N>10. e-f. Example of a building with a high settlement rate. The open white boxes in e indicate the positions of the tomo-PSInSAR scatterers. The white circles in f represent the scatterer vertical velocities, with vertical bars showing the velocity standard deviation. The surface is the best-fit 3D plane using Equation (8). Source of the 3D building model: https://github.com/ronnywang/taipei-3d-building (last accessed in August 2022). Note that the appearance of the buildings has been modified for de-identification.

10% (Figure 11b), with a high fraction for age group 80 due its limited sample size. Most of the large tilt anomalies occur in the 30 to 50 age groups (Figure 11a), with the peak tilting rate reaching 1/760 yr^{-1}. In the SPT-N > 10 group, age groups 15 to 60 have outlier fractions between 5% and 12%, with a high fraction for age group 100 due its limited sample size (Figure 11d). The youngest age group (4 years) exhibits high outlier fractions for both soil types, with some showing large tilting anomalies (Figure 11a). These elevated fractions and anomaly values may again be attributed to uneven soil compaction caused by newly constructed buildings.

Multivariable linear regression analyses reveal that, among all eligible buildings, tilting rates increase with age at a significant level but decrease with SPT-N values (model A, Table 6). However, for individual outlier tilting values, no significant linear relationship is observed with either variables (model B). When analyzed by groups among buildings aged less than 50 years, outlier fractions are not explained by age or SPT-N values either (model C). In contrast, maximum outlier tilting rates decrease with increasing SPT-N values but do not vary with age at a statistically significant level (model D). These findings suggest that while soil properties can partially explain variations in

Table 6. Coefficients and *p*-values of multivariable linear regression models for settlement and tilting.

	Settlement[a]		Tilting[b]	
	Coeff.	*p*-value	Coeff.	*p*-value
(A) Rate = $\beta_0 + \beta_1$ Age + β_2 SPT-N, All Eligible Buildings				
β_1	−0.004	3.8e-4*	−223.6	0.02*
β_2	−0.015	2.5e-7*	938.7	3.7e-4*
Model *p*-value[c]	1.9e-8*		6.6e-5*	
No. of Samples	4,199		3,638	
(B) Rate = $\beta_0 + \beta_1$ Age + β_2 SPT-N, Outliers Only				
β_1	−0.02	0.09	62.2	0.59
β_2	−0.02	0.41	83.0	0.83
Model *p*-value[c]	0.15		0.85	
No. of Samples	256		279	
(C) Outlier Fraction = $\beta_0 + \beta_1$ Age + β_2 SPT-N, using 7 Age Groups (4–50 years) and 2 SPT-N Groups[d]				
β_1	9.0e-4	0.01*	−7.8e-4	0.32
β_2	1.4e-4	0.86	6.5e-4	0.73
Model p-value[c]	0.03*		0.56	
No. of Samples	14		14	
(D) Large Outlier Rate = $\beta_0 + \beta_1$ Age + β_2 SPT-N, using 7 Age Groups (4–50 years) and 2 SPT-N Groups[e]				
β_1	0.11	0.05*	−17.3	0.54
β_2	−0.21	0.15	119.1	0.05*
Model p-value[c]	0.09		0.11	
No. of Samples	14		14	

[a]Settlement rates are expressed as increasingly positively in the regression.
[b]The denominator of the tilting rate is used in the regression. A positive coefficient indicates the variable is inversely correlated with tilting.
[c]Compared to a constant model.
[d]The mean SPT-N values are used to represent the SPT-N≤10 (mean=7.0) and SPT-N>10 (mean=19.4) groups.
[e]The 90% quantile value at each age-SPT-N group is used to represent the large outlier rates.
*Significant at an alpha level of 5%.

the maximum outlier tilting rates, additional factors are needed to account for the variability in overall outlier tilting rates and outlier fractions, consistent with the settlement analysis results.

One of the unmodeled factors could be the type or quality of building materials. The age groups 30–40, which exhibits high-rate outlier settlements or tilts, correspond to the period when a significant number of reinforced concrete buildings in Taiwan were constructed using sea sands, due to a shortage of river sands in the 1980s and 1990s (Lin et al. 1996). Based on the volume of sea sand extracted during that period, it is estimated that as many as 300,000–500,000 households, or approximately 15,000–25,000 buildings, in Taiwan may contain sea sand (Wang 2005). The extraordinarily high chloride content in sea sand can accelerate chloride-induced corrosion on the steel bar, leading to an increase in expansive stress within the surrounding concrete and the formation of cracks (Chiu, Tu, and Zhuang 2016; Lee and Cho 2009; Liu et al. 2020). This process usually degrades the performance of the reinforced concrete in a nonlinear and progressive manner (Ohtsu 2003; Weng 2016). Unfortunately, most of these sea sand buildings (or high chloride ion buildings) remain undocumented, untracked, and excluded from government-led urban regeneration plans (Lin 2019). Affected property owners are often reluctant to conduct chloride testing or structural assessments due to the concerns about potential impacts on real estate values (Lin 2019). In Section 5.5 we will discuss how SAR-based SHM analysis can be utilized to manage these vulnerable buildings.

Figure 11e,f present an example with a tilting rate of 1/1412 yr-1. The 14 scatterers associated with this building are distributed across different parts of the structure, indicating a relatively reliable assessment. At this tilting rate, the building's tilt will increase by ~1/200 over the next 7 years, and the tilt will become visually noticeable. Within 10 years, the increased tile will reach 1/100, at which point remedial action will likely be required (Charles and Skinner 2004). Figure 11 g & 11 h showcase the building with the largest number of scatterers, around 770 points in total. Most of the points come from the northeastern and southeastern facets of the twin buildings with many dihedral surfaces formed between window eaves, balcony structures, and the walls. The tilting rate is 1/35,813 per year, meaning that this young building (4 years) is very stable.

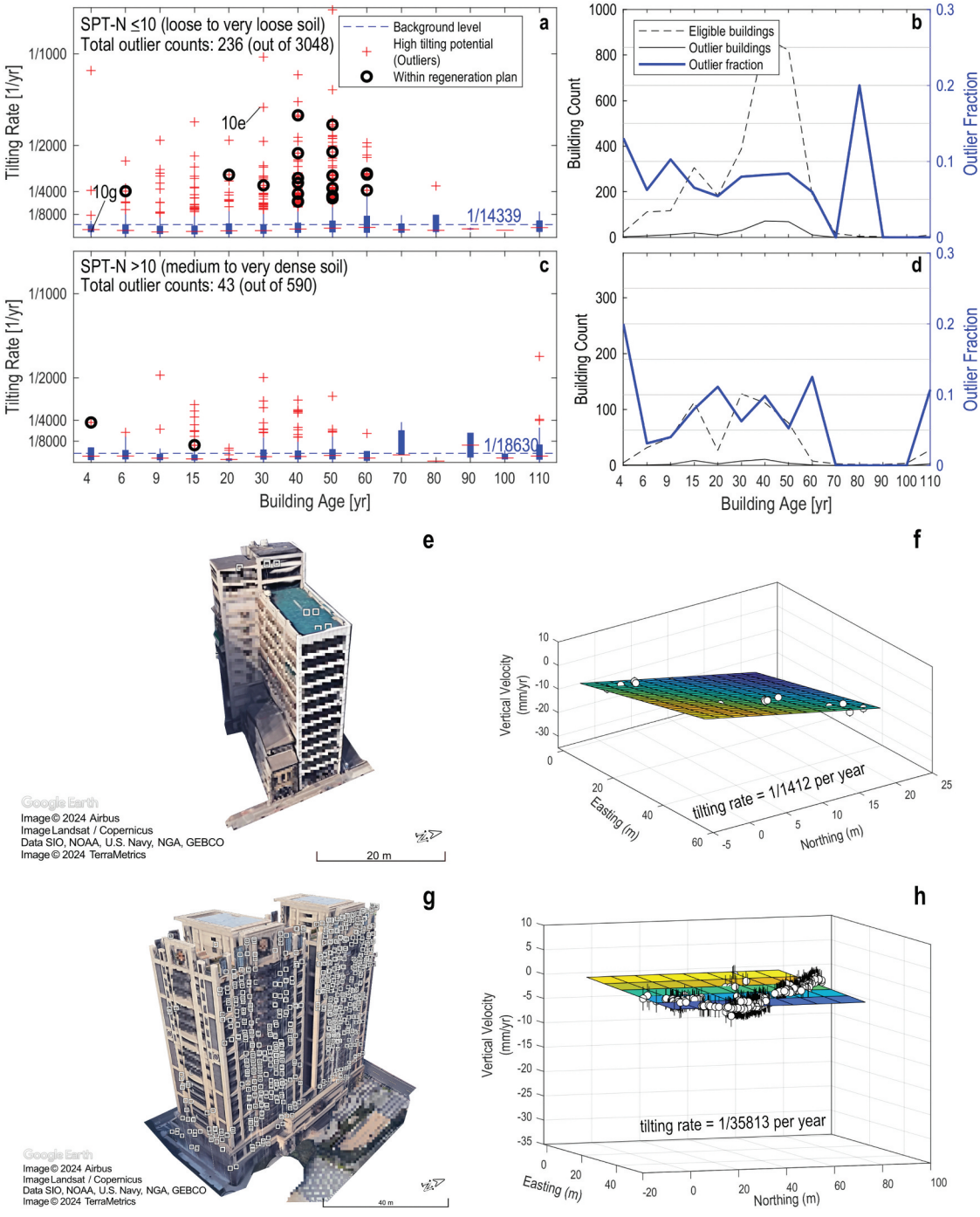

Figure 11. Boxplot statistics and example of building tilting rates at different age groups. a-b. Statistics of building tilting rates and building counts for soils with SPT-N≤10. Outliers are defined based on equation (10). c-d. Statistics for buildings on soils with SPT-N > 10. e-f. Example of a building with a high tilting rate. The open white boxes in e indicate the positions of the Tomo-PSInSAR scatterers, while the white circles in f represent the vertical velocities of the scatterers. The surface is the best-fit 3D plane using equation (8). Source of the 3D building model: google earth (last accessed in May 2024). Note that the appearance of the buildings has 42 been modified for de-identification. g-h. The building with the largest number of scatterers (770). The building age is 4 years. Source of the 3D building model: google earth (last accessed in May 2024).

5.3. SAR-based SHM validation and field observation

Validating the settlement and tilt analysis through in-situ measurements is challenging. Even if we had planned to install monitoring equipment in advance, most private property owners – particularly those with potentially problematic buildings – are reluctant to grant permission. Unfortunately, the outliers identified in our results are primarily private properties. An alternative approach could involve installing monitoring devices (possible for both GNSS stations and tiltmeters) on selected government-owned buildings. Ideally, these buildings would be evenly distributed across age groups and geographical locations. Once established, they could serve as benchmarks for validating future SAR-based SHM analyses. However, in the absence of such datasets, we need to seek alternatives to verify the occurrence of building deformation.

We first conducted a field survey to investigate buildings identified with large settlement or tilting anomalies. This survey was carried out in 2024 due to logistical reasons, and hence the time gap limits the scope for rigorous validation. The process and findings, however, can still serve as a reference for future studies or urban management practices.

For survey efficiency, we screened and identified buildings (both with and without ages) that met the following criteria: a settlement rate faster than −3 mm/yr or a tilt rate faster than 1/2000 yr^{-1}. Although empirically determined, this threshold enhances the likelihood of observing anomalous building tilt in the field, given that most concrete buildings in Taiwan have a designed lifespan of approximately 50 years and may be reconstructed afterward (Lee 2015) (Table 2). A total of 679 buildings met these two criteria. We grouped nearby anomalies into the same area, and selected 15 areas (including Dazhi) containing buildings with either clustered or unusually large anomalies. These areas are also chosen to be evenly distributed within the basin. In total, the 15 areas contain 60 buildings, comprising 20 with settlement and 40 with tilt anomalies (Table 7). At each building, we inspected visible signs of deformation, such as wall cracks, column cracks, exposed rebar, tilting relative to neighboring buildings, reinforcement measures, and evidence of rebuilding (Figure 12). Additionally, we examined the surrounding area for construction sites or newly-built steel structures.

Table 7. Field observation statistics of buildings identified with large settlement or tilting anomalies.

	Vertical Settlement*	Tilting*	Together
Number of area		15	
(A) Number of Samples	20	40	60
(B) Showing signs of deformation [B/A]	8 [40.0%]	22 [55.0%]	30 [50.0%]
(B1) Wall cracks [B1/B]	3 [37.5%]	12 [54.5%]	15 [50.0%]
(B2) Column cracks [B2/B]	1 [12.5%]	3 [13.6%]	4 [12.5%]
(B3) Rebar exposed [B3/B]	0 [0.0%]	3 [13.6%]	3 [10.0%]
(B4) Tilting [B4/B]	3 [37.5%]	8 [36.4%]	11 [36.7%]
(B5) Reinforcement [B5/B]	1 [12.5%]	1 [4.5%]	2 [6.7%]
(B6) Rebuild [B6/B]	0 [0.0%]	2 [9.1%]	2 [6.7%]
(C) No visual sign of deformation [C/A]	10 [50.0%]	13 [32.5%]	23 [38.3%]
(D) Uncertain signs or errors [D/A]	2 [10.0%]	5 [12.5%]	7 [11.7%]

*Samples are selected using the following two criteria.
Vertical settlement rate < −3 mm/yr, or tilt rate > 1/2000 yr^{-1}

Table 7 summarizes the survey results. Among the 20 buildings identified with vertical settlement anomalies, 40% exhibited signs of deformation, 50% showed no clear visual signs, and 10% has uncertain signs (e.g. minor cracks) or measurement errors (e.g. polygon errors). Of the 40 buildings with tilt anomalies, 55% exhibited signs of deformation, 32.5% showed no clear signs, and 12.5% displayed uncertain signs or measurement errors. Based on the statistics, building with tilting anomalies tends to provide more visual deformation signs than settlement anomalies. Overall, about 50% of the 60 buildings show some form of deformation or damage. While most buildings exhibited only one or two signs, the most severe case displayed up to 4 signs at the same time. Four of the 15 areas contained construction sites or newly-built steel structures, with three of these areas showing deformation in the surrounding buildings. Twenty-three buildings (38.3%) showed no signs of deformation, and 7 buildings (11.7%) exhibited uncertain signs, such as very fine cracks, or measurement errors related to the building polygon.

Our results indicate that the number of visible signs does not correlate with the magnitude of anomalies. For instance, the tilting rate of the building showing four signs is measured at 1/1,328 yr^{-1}, representing only an intermediate value among all the cases investigated. On the other hand, several buildings with larger tilting rates exhibit only one or zero signs. This result is understandable, as the absence or

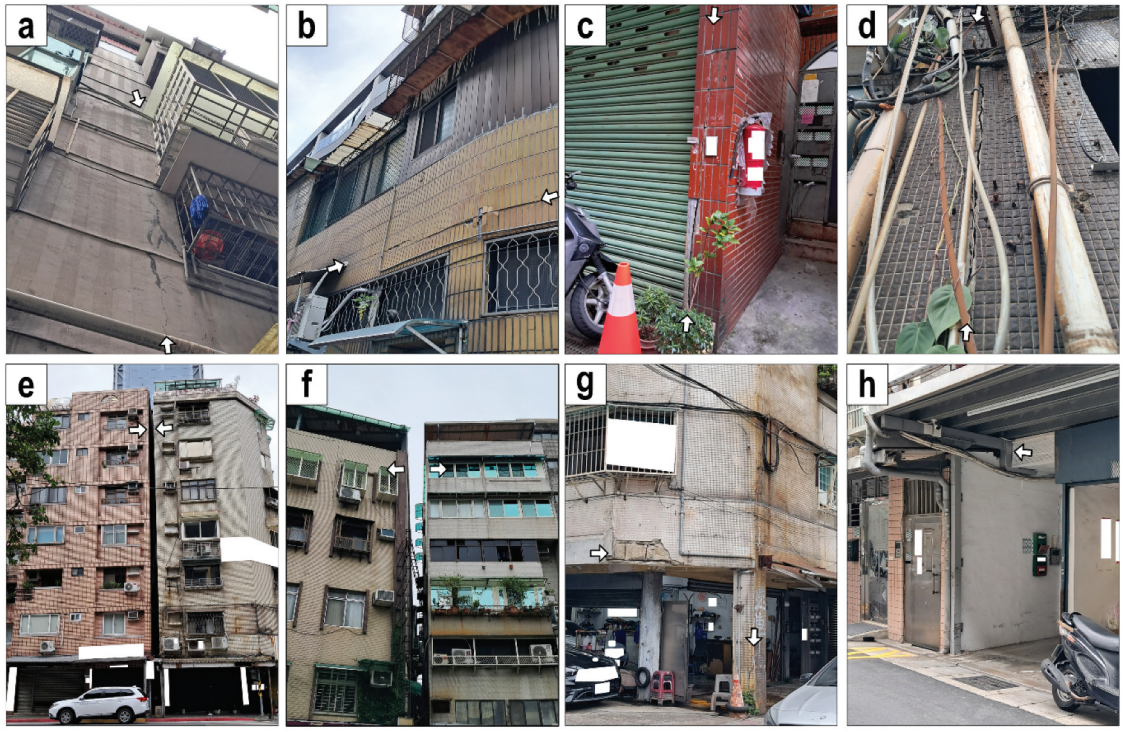

Figure 12. Examples of building deformation signs observed in the field. a. Building with vertical wall cracks. b. Building with horizontal wall cracks. c-d. Buildings with column cracks. e. Building tilting towards next building. f. Building tilting away from next building. g. Building showing exposed rebar and column crack. h. Building with reinforcement.

scarcity of visible deformation signs does not necessarily indicate a building free from any deformation. Buildings with strong structural integrity but weak foundations may appear visually intact despite undergoing subsidence or tilting. Such buildings may not require immediate remediation or retrofitting, as they might not face the same risk of collapse as those exhibiting multiple visible deformation signs. Therefore, management practices should prioritize buildings showing both deformation anomalies during SHM analysis and visual deformation signs during field surveys.

In addition to the field survey, we also obtain photos of buildings undergoing tilting restoration. One of these cases had restoration work done after the SAR sensing period, making it suitable for validating the occurrence of building tilt during the SAR acquisition period (July 2017 to October 2019) (Figure 13). The SAR-based SHM results indicate that the building on the left was tilting at a rate of 1/5,360 per year, while the building on the right remained relatively stable, tilting at a rate of 1/16,023 per year.

Finally, an unexpected chance of validation occurred on the evening of 7 September 2023, when an apartment in Dazhi, northern Taipei Basin (site E in Figure 6c) suddenly sank, turning the first floor into a basement (see news reports at https://www.taiwannews.com.tw/news/4993156 and https://focustaiwan.tw/society/202404290018, last accessed in May 2024). Several nearby buildings also exhibited varying degrees of tilting, sinking, and cracking. Investigations revealed that the incident was caused by the improper design of the foundation's diaphragm wall associated with a nearby construction site that began in 2022 (https://www.taipeitimes.com/News/taiwan/archives/2024/05/07/2003817503, last accessed in May 2024). However, previous study indicates that various types of building deformation had already occurred before 2022 (see Figure 6 in S.-Y. Lin (2022) for field photos). The high concentration of building deformation in this area is believed to be related to the extra-soft sediment from the preexisting Dadu Lake located at this site (S.-Y. Lin 2022).

The Tomo-PSInSAR results reveal an oval zone with the largest vertical velocities in the center, reaching <-10 mm/yr (Figure 14). Buildings in this area exhibit severe sinking in the center part and tilting in the periphery. According to this pattern, the coexistence of severe central settlement and peripheral tilting can serve as a strong warning sign

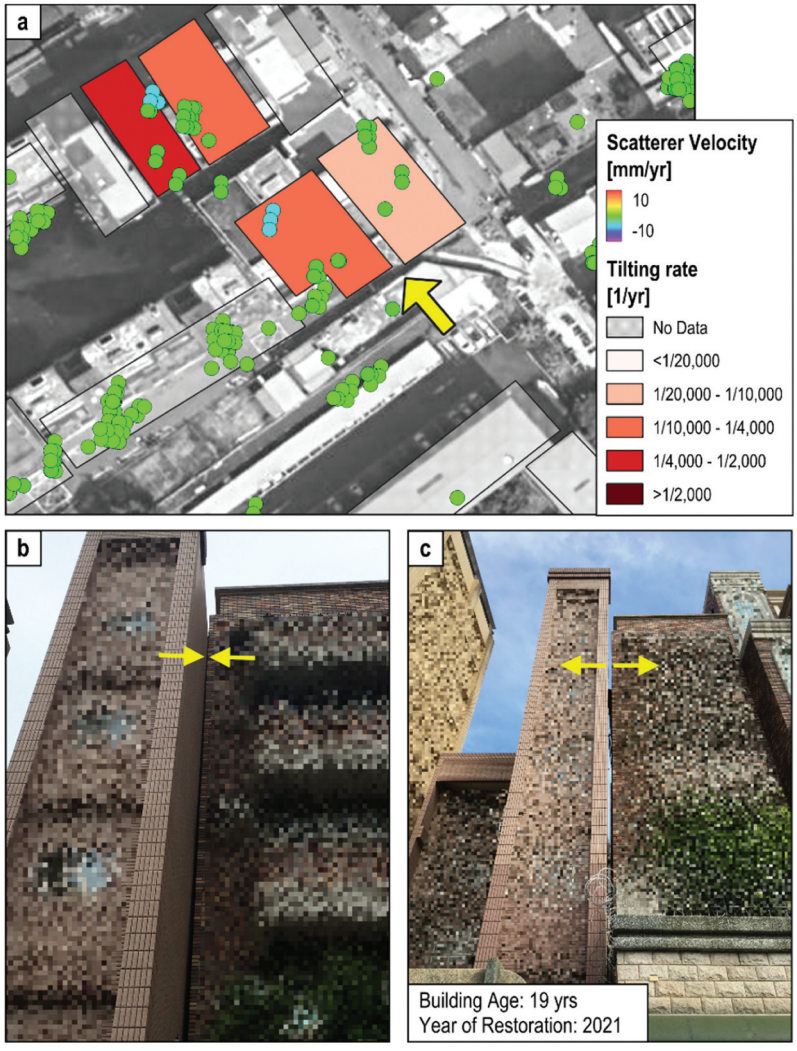

Figure 13. Example of building tilt validation. a. Map view of the validation site with building polygons color-coded according to tilting rates. The yellow arrow indicates the viewing direction of the photos in b and c. b. photo of the two buildings before tilting restoration. **c**. Photo of the two buildings after tilting restoration, completed in 2021. Note that the appearance of the buildings has been modified for de-identification.

for clusters of potentially problematic buildings. Such patterns can be detected automatically or semi-automatically through hotspot analysis techniques, such as the Getis-Ord Gi* statistic (Getis and Ord 1992) or the kernel density estimation (Chainey, Tompson, and Uhlig 2008). Preventive and targeted measures can then be implemented more effectively to mitigate further damages, particularly when there are going to be new construction projects in the area.

5.4. Overall assessment of applying SAR-based SHM to urban planning

A key objective of this work is to evaluate the effectiveness of Tomo-PSInSAR in supporting decision-making during urban planning. Section 5.2 reveals that only 11.6% (9,816 buildings) of the OSM building blocks qualify for SAR-based SHM analysis. By incorporating buildings without age information into the analysis, using the means and standard deviations of all eligible samples in Equation (7) and (10), the total number of anomalies increases to 1,058 buildings, accounting for 10.8% of the eligible buildings. Now we compute the same statistics for the buildings within current regeneration plans. These plans cover a total of 9,911 buildings (Figure 4d), of which 9.4% (930 buildings) meet the criteria for SHM analysis (Table 8). Of these, about 11.9% (111 buildings) are identified as having deformation anomalies – a proportion slightly higher than that of the entire dataset (10.8%). While the number of buildings showing

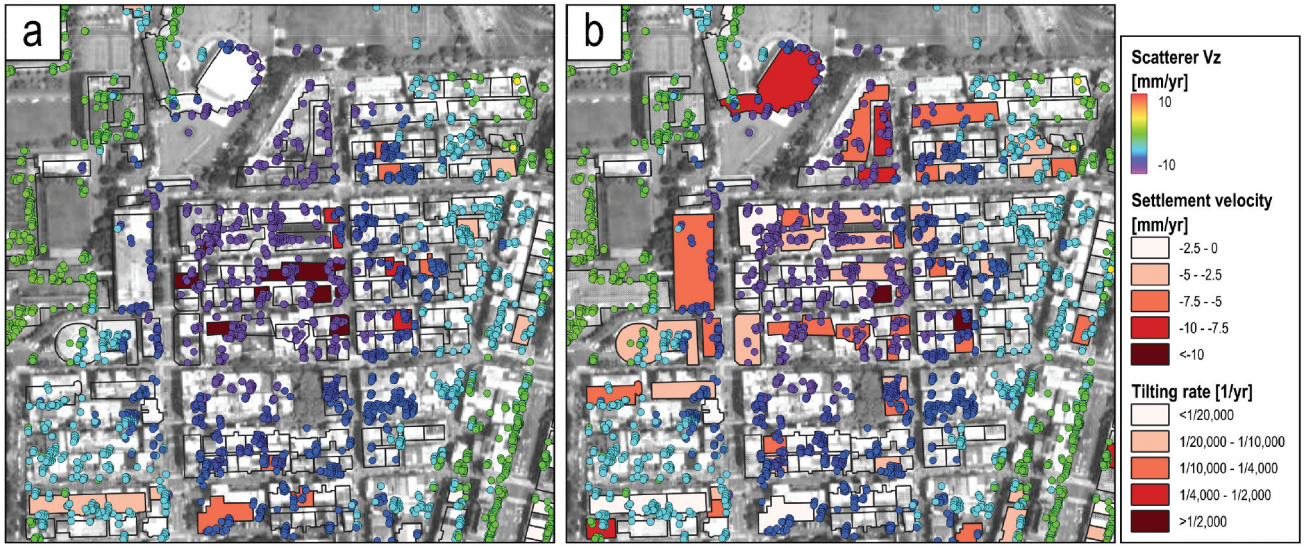

Figure 14. Building settlement and tilt in Dazhi, northern Taipei Basin. Note that the SAR images used in this study is acquired between July 2017 and October 2019, well before the incident on September 7, 2023. Refer to point E in Figure 6c for the site location. a. Building settlement. b. Building tilt. Open polygons indicate buildings not eligible for analysis.

Table 8. Statistics for applying SAR-based SHM to urban planning.

	Settlement	Tilt	Together
(A) Number of buildings in urban regeneration plans[*1]		9,911	
(B) Number of eligible buildings for analysis[*b] [B/A]	726 [7.3%]	575 [5.8%]	930 [9.4%]
(B1) With age information [B1/B]	386 [53.2%]	312 [54.3]	502 [54.0%]
(B2) Without age information [B2/B]	340 [46.8%]	263 [45.7]	428 [46.0%]
(C) Number of outliers [C/B]	48 [6.6%]	63 [11.0%]	111 [11.9%]
(C1) With age information [C1/B1]	27 [7.0%]	20 [6.4%]	47 [9.4%]
(C2) Without age information [C2/B2]	21 [6.2%]	43 [16.3%]	64 [15.0%]

[a]The buildings in the planned but not in the completed urban regeneration polygons.
[b]Refer to criteria set in Table 1.

deformation anomalies seems manageable from a practical perspective, it is based on a relatively small number of eligible buildings. If the proportion of eligible buildings increases, the number of outlier buildings may become difficult to manage. To address this point, two considerations emerge for SAR-based SHM analysis:

(1) In practice, the criteria for defining outliers in Equation (7) and (10) could be adjusted to elevate the threshold and reduce the fraction of outliers.

(2) The primary bottleneck is the low proportion of buildings eligible for the analysis, which needs to be addressed to improve scalability.

There are several factors related to the second point.

To begin, we examine the number of scatterers in each polygon. Figure 15a shows that only 41% of building polygons contain 6 or more scatterer points, while 29% of the polygons lack any. When analyzed in relation to building orientation angles, we figure that buildings with zero scatterer point are more likely oriented with their long axis pointing to the northeast (15°–75°) or southeast (135°–165°), with their within-group proportions all larger than 33% (Table 9) (Figure 16). In contrast, buildings orienting east–west (75°–105°) tend to have the lowest within group proportion of buildings with zero scatterer (22%) and the highest proportion of buildings with at least 6 scatterers (48.5%) and 10 scatterers (35%). Building orientation may also be the cause for the disproportionally lower number of eligible buildings in the SPT-N > 10 group (Table 5). The SPT-N > 10 soil group, mostly located within the New Taipei City (Figure 9), has a lower proportion of buildings oriented in the east–west direction compared to the SPT-N ≤ 10 group (26% vs. 41%, Figure 16d & 16c). All these lines of evidence suggest that building

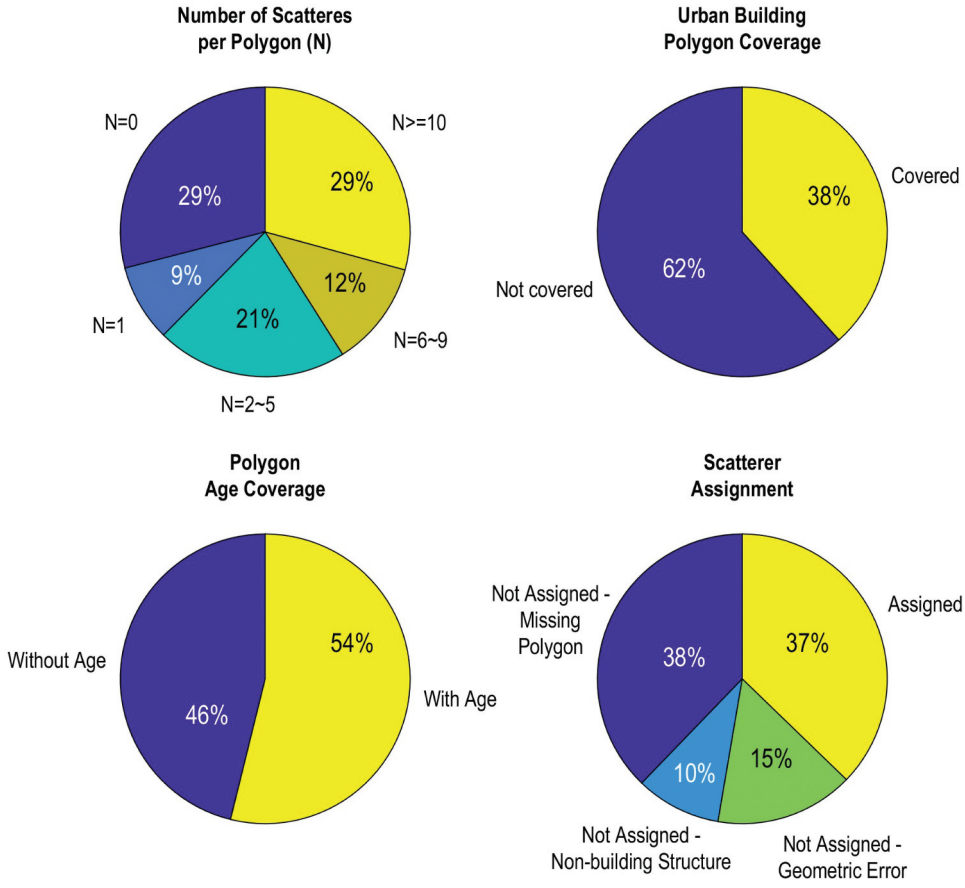

Figure 15. Statistics of factors influencing the performance of sar-based SHM analysis for urban regeneration applications. a. Distribution of the number of tomo-PSInSAR scatterers per building polygon. b. Areal coverage of urban building polygons based on the OpenStreetMap dataset (Herfort et al. 2023). c. Age coverage over the urban building polygons. d. Scatterer assignment status (see appendix a for details).

Table 9. Statistics for applying SAR-based SHM to urban planning.

Building Orientation Angle Group	Number of Scatterers Within Group Proportion [%]			
	0	1–5	6–9	≥10
−15 ~ 15°	29.5	30.9	11.5	28.0
15 ~ 45°	33.9	27.9	10.8	27.3
45 ~ 75°	34.2	31.2	10.6	24.1
75 ~ 105°	22.3	29.2	13.3	35.2
105 ~ 135°	29.4	29.1	11.5	30.0
135 ~ 165°	37.1	31.5	10.4	20.9

orientation angle contributes to the lack of scatterers for some buildings.

Next, we explore the 41% building polygons that contain at least six scatterers. Table 5 indicates that among the 41%, only 11.6% are eligible for the SHM analysis, while the remaining 29.4% fail to meet other criteria outlined in Table 1. A closer examination of the individual criteria reveals that the spatial coverage requirement accounts for 20% (or 49% of the buildings with enough scatterers) of the exclusions, leaving 9.4% of the polygons disqualified due to negative velocity constraints and RMSE in 3D plane fitting. This result highlights that an insufficient and uneven spatial distribution of scatterers within each building polygon is another key factor that limits the application of SAR-based SHM analysis.

The third factor is the low coverage rate of building polygons in the Taipei Basin. The OSM Geofabrik repository provides an areal coverage rate of only about 38% for the entire Taipei Basin (Herfort et al. 2023), leaving 62% – or approximately 2.1 million – of the Tomo-PSInSAR scatterers unanalyzed (Figure 15b). Further analysis of the scatterer assignment status reveals that, among all factors contributing to missing assignments, absent polygons still account for 34–38% of all unanalyzed points (see Appendix A for scatterer assignment analysis) (Figure 15d). Additionally, the age coverage of urban building polygons is limited, with only 54% of the buildings having age information available (Figure 15c). While age information is not

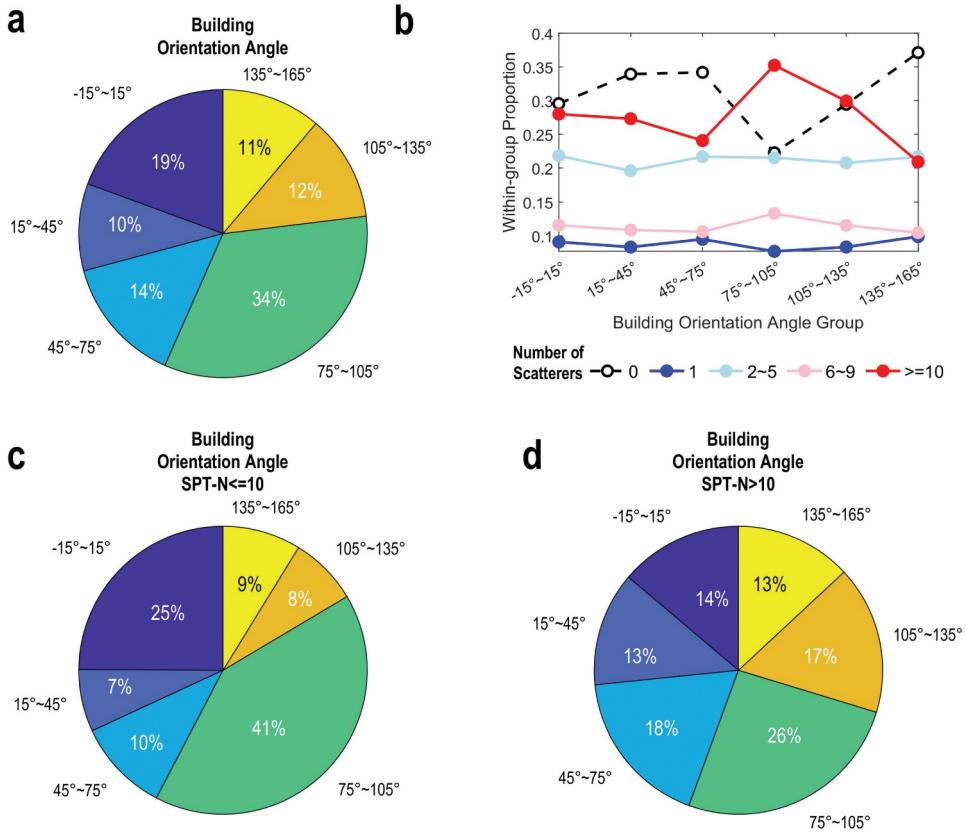

Figure 16. Effects of building orientation angles on scatterer distribution. a. Distribution of building orientation angles in the OSM building polygon dataset within the Taipei Basin. The angles are measured as the clockwise deviation of the building's long axis from due north. b. Within-group proportion of the number of scatterers across different building orientation angle groups. c. Same as subplot a for buildings with SPT-N≤10. d. Same as subplot a for buildings with SPT-N>10.

strictly required for anomaly screening, it facilitates age-dependent analysis, which helps mitigate bias caused by soil compaction associated with newly-constructed buildings.

The last factor involves geometric errors either in the buildings polygons or the scatterer locations. One issue is the overall shape and positioning of the polygons, which may be offset from their actual locations by a few meters and/or have inaccurate dimensions. Another issue is the level of details. OSM building polygons are typically simplified to rectangular shapes, whereas real building exteriors are often irregular, featuring protruding elements such as window frames, balconies, and shades. Meanwhile, the horizontal positioning bias and accuracy of scatterers have been reported at sub-meter (~18 cm) and meter level (1.2 m), respectively, based on multiview SAR tomography (Zhu et al. 2016). Since our study employs single-view tomography, we anticipate larger positioning bias and errors. These errors, compounded by inaccuracies in the building polygons, result in unsuccessful assignment of approximately one-third of the building-related scatterers (15%/(15%+37%) = 29%).

Based on the factors identified above, there are several methods that may further improve the performance. By increasing the number of scatterers per building and improving their spatial distribution and positioning accuracy, it would be beneficial to include SAR images from different viewing geometry whenever possible. Given the limitation of the DLR science proposal, this study adopts SAR images from only the right-looking geometry in a descending pass. Expanding the dataset to include both ascending and descending passes, as well as left- and right-looking geometry, would help minimize the number of blind spots, as demonstrated in Zhu et al. (2016). While obtaining images from all four viewing geometries within a single mission may not always be feasible, integrating scatterers from multiple missions with similar sensing modes could be an efficient alternative. For instance, 3-m stripmap images from

TerraSAR-X (11-day repeat cycle, 450-m orbital tube), PAZ (11 days, 500 m), and COSMO-SkyMed (16 days, 1 km) can offer compatible data for integration. Successful tomography requires consistent repeat orbit capabilities and controlled baseline dispersion levels, making most commercial small X-band satellites – such as ICEYE, Umbra, or Capella – less suitable for this purpose. Another potential approach is merging missions with different radar frequencies but similar imaging modes, such as 3-m stripmap images from the C-band RADARSAT Constellation Mission or the L-band ALOS-2/4. However, frequency-dependent scattering mechanisms – such as sensitivity to biomass and water content – may introduce variations in the detection of scatterers, particularly non-building-related ones, or their velocity estimates. Therefore, we recommend combining missions with the same radar frequencies, similar sensing modes, consistent repeat orbit capabilities, and controlled baseline dispersion to optimize multi-view tomographic geometry for more reliable SHM analysis.

Increasing the number of acquisitions and ensuring a broader distribution of spatial baselines could also improve scatterer quality and increase the number of useful points. In this work, the total perpendicular baseline span ($\Delta B_{\perp}$) and baseline standard deviation (σ_B) are 775.5 m and 15.3 m, respectively, yielding a theoretical and Cramér-Rao lower bound (CRLB) of elevation resolution at 12.1 m and 4.8 m (at SNR = 5 dB) (Table 3). More acquisitions at different geometry (larger $\Delta B_{\perp}$ and σ_B) may provide better elevation resolutions and stronger responses in normalized tomographic magnitude (NTM) during the beamforming process, allowing more scatterers to be extracted. However, we caution that more frequent visits may lead to a smaller standard deviation of the elevation aperture if the spatial baseline dispersion remains fixed, thereby reducing elevation resolution according to the CRLB (Table 3) (Zhu and Bamler 2010a). For example, if TSX acquires images consistently at an 11-day interval throughout a year, the total number of images obtained would increase to 33, compared to the current acquisition density of 18.4 images per year (41 images over 2.23 years). Consequently, the standard deviation of the elevation aperture σ_B would scale by a factor of $\sqrt{18.4/33} = 0.74$, decreasing to 11.3 m. This reduction would lead to a lower CRLB elevation resolution of 7.3 m (at SNR = 5 dB). In this case, increasing the spatial baseline dispersion simultaneously would be necessary to ensure that the higher acquisition density would effectively improve tomographic performance.

Regarding the coverage and accuracy of urban building polygons and building ages, particularly for individual buildings that are difficult to distinguish from their neighbors in nadir-view optical images due to rooftop additions, the ideal approach is to use a well-validated dataset, preferably issued by government agencies. Efforts to obtain such datasets from public sector sources are not always successful, as was the case in this study. The challenges include (1) government officials being unaware of or uncertain about the technology and its deliverable results, and (2) different perceptions regarding the sensitivity level of personal data contained in the urban building polygons. To overcome these challenges, researchers must take a proactive approach in creating connections with and gaining the trust of government officials. This can be achieved through measures such as signing memoranda of understanding between government agencies and research institutes, or involving more researchers in practical projects commissioned by government agencies. On the public sector's side, adopting a pre-commitment strategy to define the type and scope of accessible data, along with implementing access control mechanisms, can serve as viable solutions to balance open data initiatives with privacy protection (Attard et al. 2015).

5.5. Management recommendations

Although the proportion of buildings eligible for SAR-based SHM analysis shown in this study is relatively low, the detection of anomalies in 48 buildings (with and without age information; Table 8) within the current urban regeneration plans provides a substantial foundation for government authorities to develop actionable plans. Below are some recommendations on how to integrate SAR-based SHM results into the management of high-risk buildings.

Based on the magnitude of detected anomalies within the current regeneration plans, urban managers can prioritize intervention orders, focusing on buildings with higher deformation rates and/or high residential occupancy. The next step involves field investigations to assess the building's condition, as high anomaly values do not necessarily indicate poor

structural integrity, as seen in our field survey. Once verified as poor conditions in the field, SHM results combined with field observations can serve as compelling evidence to encourage property owners to undertake further inspection, such as chloride ion testing and in-situ SHM monitoring. The outcomes of these detailed assessments can then guide the decisions on rehabilitation, restoration, or reconstruction.

Specific spatial extent and clustering pattern of the anomalies may indicate potential threats to public safety. For example, the deformation pattern observed in the Dazhi case – characterized by peripheral tilting and severe central settlement in an oval-shaped zone – highlights a pattern requiring urgent attention. Preventive measures, such as implementing stricter construction regulations in nearby areas, can be deployed in advance to avoid causing more harm to already vulnerable buildings. Information on the affected area's extent and the severity should be disclosed to local residents and the construction companies.

Last but not least, given the relatively low cost of SAR-based SHM in terms of time and labor, along with its wide spatial coverage and repeatability, the analysis can be conducted regularly to track the status of identified anomalies, especially those with high values but showing no visual signs of deformation. Long-term monitoring using a consistent method will help determine whether the signals are transient, with the deformation diminishing over time, or if the situation deteriorates as deformation accumulates. The frequency of these analyses depends on the availability of high-resolution SAR images and their spatial baselines. A tradeoff exists between measurement accuracy and the temporal resolution: a longer observation period increases the number of images and improves the spatial baseline distribution for SAR tomography, but it also lengthens the interval between analyses. To achieve a better balance, urban managers could task the satellite specifically – albeit at a higher cost – to increase the number of images within a one- or two-year period. More tests and experiences will be required to determine the best solution for all relevant parameters, both technically and financially. Eventually, with a sufficient accumulation of time-series datasets, machine learning techniques can be applied for forward prediction, offering proactive insights for urban managers (Zhang et al. 2024).

6. Conclusions

By applying Tomo-PSInSAR on TerraSAR-X/TanDEM-X data for the Taipei Basin, this study demonstrates that Tomo-PSInSAR is a valuable technique for large-scale structural health monitoring (SHM). It achieves higher point density and more accurate point positions than the conventional 2D PSInSAR method. When attributed to building polygons, Tomo-PSInAR scatterer velocities can be used for deformation analysis, including building settlement and tilt. Example in the Taipei metropolitan area shows that about 11.6% of the building polygons are eligible for SHM analysis, among which 10.8% (1,058 buildings) exhibit anomalous deformation. Statistical analyses suggest that building ages and soil SPT-N values can only partially explain the outlier fractions and large outlier values. Additional unmodeled factors are needed to account for the observed variability. For example, building materials and construction quality issues – such as the sea sand buildings constructed in the 1980s and 1990s – may contribute to the high deformation anomalies observed in buildings aged 30–50 years.

When focusing on buildings within urban regeneration plans, about 9.4% are eligible for analysis, with 11.9% (111 buildings) showing anomalous deformation. The overall assessment reveals several key factors affecting the application of SAR-based SHM in urban planning: about 59% of the buildings lack a sufficient number of scatterers, 49% of the buildings with enough scatterers lack proper scatterer spatial distribution, 62% of urban area lacks building polygons, 46% of buildings lack age information, and 63% of the scatterers are not used due to various reasons. These limitations can be mitigated by incorporating SAR data from multiple viewing geometries and/or multiple missions, increasing the number of acquisitions and a broader distribution of spatial baselines, and fostering proactive collaboration with government agencies to obtain building polygon and age datasets that may have official legal validity.

Despite these constraints, the number of detectable anomalies (10.8% among all eligible buildings and 11.9% among those in urban regeneration plans), along with their magnitudes and spatial distribution, can still provide valuable supports for government agencies to develop actionable plans and prioritize regeneration efforts more effectively. To integrate the SAR-based SHM analysis into resilient

urban management, we recommend the following practices: combining SHM analysis results with field observations to justify the need for more detailed assessments, implementing preventive measures in areas exhibiting specific clustering patterns in the SHM results, and adopting a consistent, long-term monitoring approach to develop tracking capabilities and support machine learning-based predictions.

Acknowledgments

The TerraSAR-X/TanDEM-X data used in this study were provided by the German Aerospace Center (DLR) under the TerraSAR-X Archive AO project (MTH3770). The authors would like to thank Prof. Peifeng Ma and Mr Guangen Ye for their technical support in Tomo-PSInSAR. Additionally, the authors are grateful to Yu-Ting Chang and Chu-Chun Wang from National Taiwan University for their assistance with digitizing some of the datasets used in this work. This research was supported by the National Science and Technology Council under Grant 110-2119-M-001-006 and 112-2119-M-001-009 to Yunung Nina Lin. This work is IESAS contribution number 2427.

Disclosure statement

No potential conflict of interest was reported by the author(s).

Funding

The work was supported by the National Science and Technology Council [110-2119-M-001-006].

ORCID

Yunung Nina Lin http://orcid.org/0000-0002-3669-3625

Data availability statement

The data that support the findings of this study are available on request from the corresponding author, YNL, at Zenodo (https://doi.org/10.5281/zenodo.13369543). The data are not publicly available due to privacy concerns, as most datasets used and generated in this study could potentially compromise the interests of private property owners.

References

Attard, J., F. Orlandi, S. Scerri, and S. Auer. 2015. "A Systematic Review of Open Government Data Initiatives." *Government Information Quarterly* 32 (4): 399–418. https://doi.org/10.1016/j.giq.2015.07.006.

Auld, H., J. Klaassen, and N. Comer. 2006. "Weathering of Building Infrastructure and the Changing Climate: Adaptation Options." In, *2006 IEEE EIC Climate Change Conference*, Ottawa, Canada, p. 1–11.

Balageas, D., C.-P. Fritzen, and A. Güemes. 2006. Structural Health Monitoring. Wiley.

Belousov, A., M. Belousova, C.-H. Chen, and G. F. Zellmer. 2010. "Deposits, Character and Timing of Recent Eruptions and Gravitational Collapses in Tatun Volcanic Group, Northern Taiwan: Hazard-Related Issues." *Journal of Volcanology and Geothermal Research* 191 (3–4): 205–221. https://doi.org/10.1016/j.jvolgeores.2010.02.001.

Budillon, A., and G. Schirinzi. 2022. "Remote Monitoring of Civil Infrastructure Based on TomoSAR. in." *Infrastructures* 7 (4): 52. https://doi.org/10.3390/infrastructures7040052.

Burbey, T. J. 2006. "Three-Dimensional Deformation and Strain Induced by Municipal Pumping, Part 2: Numerical Analysis." *Journal of Hydrology* 330 (3–4): 422–434. https://doi.org/10.1016/j.jhydrol.2006.03.035.

Central Geological Survey. 2020. *The Introduction of Urban Geotechnical Environmental Geological Map (I)*. Taipei: Central Geological Survey.

Cerchiello, V., G. Tessari, E. Velterop, P. Riccardi, M. Defilippi, and P. Pasquali. 2017. "Building Damage Risk by Modeling Interferometric Time Series." *IEEE Geoscience & Remote Sensing Letters* 14 (4): 509–513. https://doi.org/10.1109/LGRS.2017.2651938.

Chainey, S., L. Tompson, and S. Uhlig. 2008. "The Utility of Hotspot Mapping for Predicting Spatial Patterns of Crime." *Security Journal* 21 (1–2): 4–28. https://doi.org/10.1057/palgrave.sj.8350066.

Chan, C.-H., K.-F. Ma, J. B. H. Shyu, Y.-T. Lee, Y.-J. Wang, J.-C. Gao, Y.-T. Yen, and R.-J. Rau. 2020. "Probabilistic Seismic Hazard Assessment for Taiwan: TEM PSHA2020." *Earthquake Spectra* 36 (1_suppl): 137–159. https://doi.org/10.1177/8755293020951587.

Charles, J. A., and H. D. Skinner. 2004. "Settlement and Tilt of Low-Rise Buildings." *Proceedings of the Institution of Civil Engineers - Geotechnical Engineering*, *157*, 65–75.

Chen, C.-H., and S.-B. Lin. 2002. "Eruptions Younger Than 20 Ka of the Tatun Volcano Group as Viewed from the Sediments of the Sungshan Formation in Taipei Basin." *Western Pacific Earth Sciences* 2 (2): 191–204. https://wpes.gst.org.tw/cht/periodical_detial.php?s=87.

Chen, C.-T., J.-C. Hu, C.-Y. Lu, J.-C. Lee, and Y.-C. Chan. 2007. "Thirty-Year Land Elevation Change from Subsidence to Uplift Following the Termination of Groundwater Pumping and Its Geological Implications in the Metropolitan Taipei Basin, Northern Taiwan." *Engineering Geology* 95 (1–2): 30–47. https://doi.org/10.1016/j.enggeo.2007.09.001.

Chen, F., H. Xu, W. Zhou, W. Zheng, Y. Deng, and I. Parcharidis. 2021. "Three-Dimensional Deformation Monitoring and Simulations for the Preventive Conservation of Architectural Heritage: A Case Study of the Angkor Wat Temple, Cambodia." *GIScience & Remote Sensing* 58 (2): 217–234. https://doi.org/10.1080/15481603.2020.1871188.

Chen, F., W. Zhou, C. Chen, and P. Ma. 2019. "Extended D-TomoSAR Displacement Monitoring for Nanjing (China) City Built Structure Using High-Resolution TerraSAR/tanDEM-X and Cosmo SkyMed SAR Data." *Remote Sensing* 11 (22): 2623. https://doi.org/10.3390/rs11222623.

Chen, W.-S., C.-C. Lin, C.-C. Yang, L.-Y. Fei, K.-S. Shea, H.-M. Kung, P.-Y. Lin, and H.-C. Yang. 2008. "The Temporal and Spatial Evolution of Sedimentary Sequence Framework and Tectonics of the Taipei Basin Since the Late-Pleistocene." *Bulletin of the Central Geological Survey* 21:61–106. https://twgeoref.gsmma.gov.tw/GipOpenWeb/imgAction?f=/2008/20082144/0001.pdf.

Chen, X., J. Peng, and H. Yang. 2017. "Orbital Error Modeling and Analysis of Spaceborne In SAR." In *2017 SAR in Big Data Era: Models, Methods and Applications (BIGSARDATA)*, 1–6.

Cheng, C.-T., C.-T. Lee, P.-S. Lin, B.-S. Lin, Y.-B. Tsai, and S.-J. Chiou. 2010. "Probabilistic Earthquake Hazard in Metropolitan Taipei and Its Surrounding Regions." *Terrestrial Atmospheric and Oceanic Sciences* 21 (3): 429–446. https://doi.org/10.3319/TAO.2009.11.11.01(TH).

Chiu, C.-K., F.-C. Tu, and Y.-T. Zhuang. 2016. "Reliability-Based Design Method of Suppressing Chloride Ingress for Reinforced Concrete Buildings Located in Coastal Regions of Taiwan." *Structure and Infrastructure Engineering* 12 (2): 188–207. https://doi.org/10.1080/15732479.2014.1002793.

Chmutina, K., T. Ganor, and L. Bosher. 2014. "Role of Urban Design and Planning in Disaster Risk Reduction." *Proceedings of the Institution of Civil Engineers - Urban Design and Planning 167*, 125–135. https://doi.org/10.1680/udap.13.00011 .

Ciampalini, A., L. Solari, R. Giannecchini, Y. Galanti, and S. Moretti. 2019. "Evaluation of Subsidence Induced by Long-Lasting Buildings Load Using InSAR Technique and Geotechnical Data: The Case Study of a Freight Terminal (Tuscany, Italy)." *International Journal of Applied Earth Observation and Geoinformation* 82:101925. https://doi.org/10.1016/j.jag.2019.101925.

Drougkas, A., E. Verstrynge, K. Van Balen, M. Shimoni, T. Croonenborghs, R. Hayen, and P.-Y. Declercq. 2020a. "Country-Scale InSAR Monitoring for Settlement and Uplift Damage Calculation in Architectural Heritage Structures." *Structural Health Monitoring* 20 (5): 2317–2336. https://doi.org/10.1177/1475921720942120.

Economic and Social Commission for Asia and the Pacific. 2023. *Crisis Resilient Urban Futures: The Future of Asian & Pacific Cities 2023*. Incheon: United Nations.

Farr, T. G., P. A. Rosen, E. Caro, R. Crippen, R. Duren, S. Hensley, M. Kobrick, et al. 2007. "The Shuttle Radar Topography Mission." *Reviews of Geophysics* 45 (2): 1–33. https://doi.org/10.1029/2005RG000183.

Ferretti, A., C. Prati, and F. Rocca. 2000. "Nonlinear Subsidence Rate Estimation Using Permanent Scatterers in Differential SAR Interferometry." *IEEE Transactions on Geoscience & Remote Sensing* 38 (5): 2202–2212. https://doi.org/10.1109/36.868878.

Ferretti, A., C. Prati, and F. Rocca. 2001. "Permanent Scatterers in SAR Interferometry." *IEEE Transactions on Geoscience & Remote Sensing* 39 (1): 8–20. https://doi.org/10.1109/36.898661.

Fiaschi, S., and S. Wdowinski. 2020. "Local Land Subsidence in Miami Beach (FL) and Norfolk (VA) and Its Contribution to Flooding Hazard in Coastal Communities Along the U.S. Atlantic Coast." *Ocean & Coastal Management* 187:105078. https://doi.org/10.1016/j.ocecoaman.2019.105078.

Fletcher, J. B., and K.-L. Wen. 2005. "Strong Ground Motion in the Taipei Basin from the 1999 Chi-Chi, Taiwan, Earthquake." *Bulletin of the Seismological Society of America* 95 (4): 1428–1446. https://doi.org/10.1785/0120040022.

Fornaro, G., and V. Pascazio. 2014. "Chapter 20 - SAR Interferometry and Tomography: Theory and Applications." In *Academic Press Library in Signal Processing*, edited by N. D. Sidiropoulos, F. Gini, R. Chellappa, and S. Theodoridis, pp. 1043–1117. Oxford, UK: Elsevier.

Fornaro, G., D. Reale, A. Pauciullo, X. X. Zhu, and R. Bamler. 2012. "SAR Tomography: An Advanced Tool for Spaceborne 4D Radar Scanning with Application to Imaging and Monitoring of Cities and Single Buildings." *IEEE Geoscience and Remote Sensing Newsletter*, 9–17.

Galloway, D., D. R. Jones, and S. E. Ingebritsen. 1999. *Land Subsidence in the United States*. Denver, Colorado: USGS.

Getis, A., and J. K. Ord. 1992. "The Analysis of Spatial Association by Use of Distance Statistics." *Geographical Analysis* 24 (3): 189–206. https://doi.org/10.1111/j.1538-4632.1992.tb00261.x.

Giardina, G., P. Milillo, M. J. DeJong, D. Perissin, and G. Milillo. 2019. "Evaluation of InSAR Monitoring Data for Post-Tunnelling Settlement Damage Assessment." *Structural Control & Health Monitoring* 26 (2): e2285. https://doi.org/10.1002/stc.2285.

Gielen, E., G. Riutort-Mayol, J. L. Miralles i Garcia, and J. S. Palencia Jiménez. 2019. "Cost Assessment of Urban Sprawl on Municipal Services Using Hierarchical Regression." *Environment & Planning B: Urban Analytics & City Science* 48 (2): 280–297. https://doi.org/10.1177/2399808319869345.

Hanssen, R. F. 2001. *Radar Interferometry, Data Interpretation and Error Analysis*. New York: Springer.

Herfort, B., S. Lautenbach, J. Porto de Albuquerque, J. Anderson, and A. Zipf. 2023. "A Spatio-Temporal Analysis Investigating Completeness and Inequalities of Global Urban Building Data in OpenStreetmap." *Nature Communications* 14 (1): 3985. https://doi.org/10.1038/s41467-023-39698-6.

Hooper, A., P. Segall, and H. Zebker. 2007. "Persistent Scatterer Interferometric Synthetic Aperture Radar for Crustal Deformation Analysis, with Application to Volcán Alcedo, Galápagos." *Journal of Geophysical Research Solid Earth* 112 (B7). https://doi.org/10.1029/2006JB004763.

Hooper, A., H. Zebker, P. Segall, and B. Kampes. 2004. "A New Method for Measuring Deformation on Volcanoes and Other Natural Terrains Using InSAR Persistent Scatterers." *Geophysical Research Letter* 31 (23). https://doi.org/10.1029/2004GL021737.

Hu, J., K. Zhu, H. Fu, J. Liu, C. Wang, and R. Gui. 2022. "Isolating Orbital Error from Multitemporal InSAR Derived Tectonic Deformation Based on Wavelet and Independent Component Analysis." *IEEE Geoscience & Remote Sensing Letters* 19:1–5. https://doi.org/10.1109/LGRS.2022.3185147.

Huang, S.-Y., C. M. Rubin, Y.-G. Chen, and H.-C. Liu. 2007. "Prehistoric Earthquakes Along the Shanchiao Fault, Taipei Basin, Northern Taiwan." *Journal of Asian Earth Sciences* 31 (3): 265–276. https://doi.org/10.1016/j.jseaes.2006.07.025.

Huber, P. J. 1964. "Robust Estimation of a Location Parameter." *Annals of Mathematical Statistics* 35 (1): 73–101. https://doi.org/10.1214/aoms/1177703732.

Japanese Road Association. 1996. *Specification for Highway Bridges, Part V, Seismic Design*. Tokyo, Japan: NIPPAN.

Katz, D. S. W., and S. A. Batterman. 2019. "Allergenic Pollen Production Across a Large City for Common Ragweed (Ambrosia artemisiifolia)." *Landscape and Urban Planning* 190:103615. https://doi.org/10.1016/j.landurbplan.2019.103615.

Lee, H.-S., and Y.-S. Cho. 2009. "Evaluation of the Mechanical Properties of Steel Reinforcement Embedded in Concrete Specimen as a Function of the Degree of Reinforcement Corrosion." *International Journal of Fracture* 157 (1–2): 81–88. https://doi.org/10.1007/s10704-009-9334-7.

Lee, S.-M., W.-L. Wu, H.-C. Li, C.-Y. Yang, W.-C. Hsieh, C.-H. Hsu, C.-C. Tseng, C.-P. Wang, H.-P. Lin, and M.-C. Sung. 2011. "The Geological Evolution of the Taipei Basin." In *The Geology and Geohazard Prevention for the Taipei Basin*, edited by L.-Y. Fei. New Taipei City: Central Geological Survey, p. 14–43.

Lee, W.-W. 2015. "Preliminary Study on Improving the Long-Term Quality and Function of Building Construction." *Architecture and Building Research Institute*, Ministry of the Interior.

Lin, C.-H. 2017. "Probable Dynamic Triggering of Phreatic Eruption in the Tatun Volcano Group of Taiwan." *Journal of Asian Earth Sciences* 149:78–85. https://doi.org/10.1016/j.jseaes.2017.01.023.

Lin, C.-Y. 2019. Discussion on the Reconstruction Issues of High Chloride Ion Building in Taipei City." Master thesis. National Cheng Chi University. https://hdl.handle.net/11296/573v65 .

Lin, S.-Y. 2022. "Urban Hazards Caused by Ground Deformation and Building Subsidence Over Fossil Lake Beds: A Study from Taipei City." *Geomatics, Natural Hazards and Risk* 13 (1): 2890–2910. https://doi.org/10.1080/19475705.2022.2141139.

Lin, W.-M., C.-L. Hwang, Y.-N. Peng, and I.-Y. Wu. 1996. "Analysis and Investigation of Sea Sand Buildings." *Journal of Chinese Corrosion Engineering* 10 (2): 92–108. https://doi.org/10.6376/JCCE.199606.0092.

Liu, Q., R. K. L. Su, C.-Q. Li, K. Shih, and C. Liao. 2020. "In-Situ Deformation Modulus of Rust in Concrete Under Different Levels of Confinement and Rates of Corrosion." *Construction and Building Materials* 255:119369. https://doi.org/10.1016/j.conbuildmat.2020.119369.

Ma, P., and H. Lin. 2016. "Robust Detection of Single and Double Persistent Scatterers in Urban Built Environments." *IEEE Transactions on Geoscience & Remote Sensing* 54 (4): 2124–2139. https://doi.org/10.1109/TGRS.2015.2496193.

Ma, P., H. Lin, H. Lan, and F. Chen. 2015. "Multi-Dimensional SAR Tomography for Monitoring the Deformation of Newly Built Concrete Buildings." *ISPRS Journal of Photogrammetry & Remote Sensing* 106:118–128. https://doi.org/10.1016/j.isprsjprs.2015.04.012.

Macchiarulo, V., P. Milillo, M. J. DeJong, J. González Martí, J. Sánchez, and G. Giardina. 2021. "Integrated InSAR Monitoring and Structural Assessment of Tunnelling-Induced Building Deformations." *Structural Control & Health Monitoring* 28 (9): e2781. https://doi.org/10.1002/stc.2781.

Nguyen, M., Y. N. Lin, Q. C. Tran, C.-F. Ni, Y.-C. Chan, K.-H. Tseng, and C.-P. Chang. 2022. "Assessment of Long-Term Ground Subsidence and Groundwater Depletion in Hanoi, Vietnam." *Engineering Geology* 299:106555. https://doi.org/10.1016/j.enggeo.2022.106555.

Ohtsu, M. 2003. "Detection and Identification of Concrete Cracking in Reinforced Concrete by Acoustic Emission." *AIP Conference Proceedings*, *657*, 1455–1462.

Pacione, M. 2005. *Urban Geography: A Global Perspective*. 2nd ed. London: Roiutledge.

Pu, H. C., C. H. Lin, Y. C. Lai, M. H. Shih, L. C. Chang, H. F. Lee, P. T. Lee, et al. 2020. "Active Volcanism Revealed from a Seismicity Conduit in the Long-Resting Tatun Volcano Group of Northern Taiwan." *Scientific Reports* 10 (1): 6153. https://doi.org/10.1038/s41598-020-63270-7.

Rai, G. 2024. "Challenges in Structural Health Monitoring and Rehabilitation." *Civil Engineering & Construction Review* 37:1–18. https://info.cecr.in/challenges-in-structural-health-monitoring-and-rehabilitation/.

Reale, D., G. Fornaro, and A. Pauciullo. 2013. "Extension of 4-D SAR Imaging to the Monitoring of Thermally Dilating Scatterers." *IEEE Transactions on Geoscience & Remote Sensing* 51:5296–5306. https://doi.org/10.1109/TGRS.2012.2233205.

Reigber, A., and A. Moreira. 2000. "First Demonstration of Airborne SAR Tomography Using Multibaseline L-Band Data." *IEEE Transactions on Geoscience & Remote Sensing* 38 (5): 2142–2152. https://doi.org/10.1109/36.868873.

Rodríguez-Antuñano, I., B. Barros, J. Martínez-Sánchez, and B. Riveiro. 2024. "Urban Infrastructure Vulnerability to Climate-Induced Risks: A Probabilistic Modeling Approach Using Remote Sensing as a Tool in Urban Planning. in." *Infrastructures* 9 (7): 107. https://doi.org/10.3390/infrastructures9070107.

Rodríguez-Antuñano, I., J. Martínez-Sánchez, M. Cabaleiro, and B. Riveiro. 2023. "Anticipating the Collapse of Urban Infrastructure: A Methodology Based on Earth Observation and MT-InSAR." *In, Remote Sensing* 15 (15): 3867. https://doi.org/10.3390/rs15153867.

Rodríguez-Antuñano, I., J. Martínez-Sánchez, S. Lagüela-López, and B. Riveiro. 2022. "Towards More Resilient Smart Cities: MT-InSAR Monitoring of Urban Infrastructure Using Machine Learning Techniques." *ISPRS Annals of the Photogrammetry, Remote Sensing & Spatial Information Sciences* X-4/W3-2022:

X-4/W3–2022, 221–228. https://doi.org/10.5194/isprs-annals-X-4-W3-2022-221-2022.

Sharifi, A., and Y. Yamagata. 2014. "Resilient Urban Planning: Major Principles and Criteria." *Energy Procedia* 61:1491–1495. https://doi.org/10.1016/j.egypro.2014.12.154.

Shyu, J. B. H., Y.-H. Yin, C.-H. Chen, Y.-R. Chuang, and S.-C. Liu. 2020. "Updates to the On-Land Seismogenic Structure Source Database by the Taiwan Earthquake Model (TEM) Project for Seismic Hazard Analysis of Taiwan." *Terrestrial Atmospheric and Oceanic Sciences* 31 (4): 469–478. https://doi.org/10.3319/TAO.2020.06.08.01.

Simons, M., and P. A. Rosen. 2015. "3.12 - Interferometric Synthetic Aperture Radar Geodesy." In *Treatise on Geophysics*, *(Second Edition)* Edited by G. Schubert, 339–385. Oxford: Elsevier.

Stewart, M. G., X. Wang, and M. N. Nguyen. 2012. "Climate Change Adaptation for Corrosion Control of Concrete Infrastructure." *Structural Safety* 35:29–39. https://doi.org/10.1016/j.strusafe.2011.10.002.

Teng, L. S., C. T. Lee, C.-H. Peng, W.-F. Chen, and C.-J. Chu. 2001. "Origin and Geological Evolution of the Taipei Basin, Northern Taiwan." *Western Pacific Earth Sciences* 1 (2): 115–142. https://wpes.gst.org.tw/cht/periodical_detial.php?s=83 .

Terzaghi, K., R. B. Peck, and G. Mesri. 1996. *Soil Mechanics in Engineering Practice*. Third Edition ed. New York: John WIley & Sons, Inc.

Tu, Y.-H., K.-M. Huang, F.-L. Chou, W.-C. Chiang, and C.-I. Lin. 2011. "A Comparative Study on the Reasonableness of Different Survey Transect Types for Measuring Building Tilt." *Engineering Times* 823.

Tung, H., H.-Y. Chen, J.-C. Hu, K.-E. Ching, H. Chen, and K.-H. Yang. 2016. "Transient Deformation Induced by Groundwater Change in Taipei Metropolitan Area Revealed by High Resolution X-Band SAR Interferometry." *Tectonophysics* 692:265–277. https://doi.org/10.1016/j.tecto.2016.03.030.

United Nations, D. O. E. A. S. A., and Population Division. 2019. *World Urbanization Prospects: The 2018 Revision*. New York: The United Nations.

van der Horst, T., M. M. Rutten, N. C. van de Giesen, and R. F. Hanssen. 2018. "Monitoring Land Subsidence in Yangon, Myanmar Using Sentinel-1 Persistent Scatterer Interferometry and Assessment of Driving Mechanisms." *Remote Sensing of Environment* 217:101–110. https://doi.org/10.1016/j.rse.2018.08.004.

Wang, C.-Y., Y.-H. Lee, M.-L. Ger, and Y.-L. Chen. 2004. "Investigating Subsurface Structures and P- and S-Wave Velocities in the Taipei Basin." *Terrestrial Atmospheric and Oceanic Sciences* 15 (4): 609–627. https://doi.org/10.3319/TAO.2004.15.4.609(T).

Wang, S.-C. 2005. "Research on the Integration of Legal Systems for Repair, Renovation, and Reconstruction After Structural Damage to Buildings." New Taipei City: Architecture and Building Research Institute, Ministry of the Interior, p. 107. Architecture and Building Research Institute.

Wellmann, T., A. Lausch, E. Andersson, S. Knapp, C. Cortinovis, J. Jache, S. Scheuer, et al. 2020. "Remote Sensing in Urban Planning: Contributions Towards Ecologically Sound Policies?" *Landscape and Urban Planning* 204:103921. https://doi.org/10.1016/j.landurbplan.2020.103921

Weng, T.-L. 2016. "A Risk Assessment Model for Buildings of Reinforced Concrete Containing High Concentration of Chloride Ions." *Journal of Marine Science and Technology* 24 (5): 1016–1025. https://doi.org/10.6119/JMST-016-0913-2.

Wu, P., M. M. Wei, J.-C. Hu, S. D'Hondt, H. Tung, S.-H. Lin, and C. Russoniello. 2024. "Dynamic Vertical Land Motion Driven by Climate and Humans in the Metropolitan Taipei Basin." http://dx.doi.org/10.2139/ssrn.5041283.

Yang, Q., Y. Ke, D. Zhang, B. Chen, H. Gong, M. Lv, L. Zhu, and X. Li. 2018. "Multi-Scale Analysis of the Relationship Between Land Subsidence and Buildings: A Case Study in an Eastern Beijing Urban Area Using the PS-InSAR Technique." *In Remote Sensing* 10 (7): 1006. https://doi.org/10.3390/rs10071006.

Yu, D., B. Xun, P. Shi, H. Shao, and Y. Liu. 2012. "Ecological Restoration Planning Based on Connectivity in an Urban Area." *Ecological Engineering* 46:24–33. https://doi.org/10.1016/j.ecoleng.2012.04.033.

Zhang, J., P. Kou, Y. Tao, Z. Jin, Y. Huang, J. Cui, W. Liang, and R. Liu. 2024. "Urban Ground Subsidence Monitoring and Prediction Using Time-Series InSAR and Machine Learning Approaches: A Case Study of Tianjin, China." *Environmental Earth Sciences* 83 (16): 473. https://doi.org/10.1007/s12665-024-11778-w.

Zhang, L., X. Ding, Z. Lu, H. S. Jung, J. Hu, and G. Feng. 2014. "A Novel Multitemporal InSAR Model for Joint Estimation of Deformation Rates and Orbital Errors." *IEEE Transactions on Geoscience & Remote Sensing* 52 (6): 3529–3540. https://doi.org/10.1109/TGRS.2013.2273374.

Zhu, X. X., and R. Bamler. 2010a. "Tomographic SAR Inversion by L_1 -Norm Regularization—The Compressive Sensing Approach." *IEEE Transactions on Geoscience & Remote Sensing* 48 (10): 3839–3846. https://doi.org/10.1109/TGRS.2010.2048117.

Zhu, X. X., and R. Bamler. 2010b. "Very High Resolution Spaceborne SAR Tomography in Urban Environment." *IEEE Transactions on Geoscience & Remote Sensing* 48 (12): 4296–4308. https://doi.org/10.1109/TGRS.2010.2050487.

Zhu, X. X., S. Montazeri, C. Gisinger, R. F. Hanssen, and R. Bamler. 2016. "Geodetic SAR Tomography." *IEEE Transactions on Geoscience & Remote Sensing* 54 (1): 18–35. https://doi.org/10.1109/TGRS.2015.2448686.

Zhu, Z., Y. Zhou, K. C. Seto, E. C. Stokes, C. Deng, S. T. A. Pickett, and H. Taubenböck. 2019. "Understanding an Urbanizing Planet: Strategic Directions for Remote Sensing." *Remote Sensing of Environment* 228:164–182. https://doi.org/10.1016/j.rse.2019.04.020.

Appendix

Appendix A. Scatterer missing assessment analysis

To perform SHM analysis, scatterers must be assigned to specific polygons. However, among the ~3.3 million scatterer points identified by Tomo-PSInSAR, only ~1.2 million (~37%) are successfully matched to an OSM polygon. This means that 63% of the scatterers are not assigned and hence not used in the analysis. Several factors contribute to the missing assignments, including 1) missing polygons, 2) scatterers originating from non-building structures (e.g., bridges, light poles), and 3) geometric inaccuracies in either the building polygons or the scatterers. In particular, since building polygons do not always capture precise positions or irregular outer wall geometries, some scatterers are inevitably omitted during assignment.

Estimating the relative contribution of these factors is challenging due to the spatial inhomogeneity of building polygons. In regions with numerous missing polygons, it is difficult to isolate the proportion of missing assignments caused by geometric inaccuracies from that of missing polygons. To address this issue, we select areas where building polygons are relatively complete and estimate the proportion of non-building-related scatterers and geometry errors. Assuming the mean proportions from these areas are representative, we estimate the proportion of missing assignments due to absent polygons by subtracting the other two from the overall 63% missing rate.

For this analysis, we manually select 15 areas with well-covered building polygons, spanning various urban and infrastructural settings—including residential zones, school districts, parks, car parks, an airport, viaducts, and bridges (Table A1) (Figure A1). Within these areas, we identify scatterers lacking OSM assignments and visually classify their exclusion reasons. Scatterers linked to missing polygons (only a few) or non-building structures are also identified by comparing their locations with buildings shown on optical satellite imagery. Geometric errors in either the polygons or scatterers are assessed based on their alignment with and distance to polygon edges, typically appearing as small offset (<3–5 meters).

Table A1 summarizes the results for each area. To determine representative proportions for missing assignments due to geometric errors and non-building-related scatterers, we first exclude scatterers unassigned due to absent polygons. We then compute these two proportions per area and average them over all areas and all scatterers, respectively. If we adopt the area-based mean values as the representative proportions, the estimated proportion of missing assignments due to absent polygons is 63%–13.1%-16.2% = 33.7%. Alternatively, if we adopt the mean over all scatterers as the representative proportions, the estimated proportion of missing assignments due to absent polygons is 63%–15.5%–9.5% = 38%. The latter value is adopted in Figure 15d.

Table A1. Missing assignment analysis for scatterers within selected areas with relatively complete urban polygons.

Area ID	Area Size [km^2]	Total Number of Scatterers (A)	Scatterers Assigned (B)	Scatterers Not Assigned (C)			Features in Area*
				(C1) Geometric Error	(C2) Non-building	(C3) Missing Polygon	
1	0.25	5065	4238	765	1	61	R, S, P, PC
2	0.35	5602	4922	668	7	5	R
3	1.85	4354	2473	506	1014	361	A, CP
4	0.33	6741	5978	676	7	80	R
5	0.28	6410	5180	993	176	61	R, P, B
6	030	1075	344	1	730	0	P, V
7	0.14	3559	2375	1002	39	143	R, P
8	1.97	1364	5	0	1359	0	B
9	0.15	3364	2848	364	86	66	P
10	0.44	9517	7268	1185	125	939	R, S, P
11	0.21	4798	3409	941	5	443	R, P
12	0.17	2715	2500	0	57	158	R, S, CP
13	0.18	3496	2361	498	256	381	R, P, CP
14	1.06	15889	11526	2415	1600	348	R, S, P, CP, B
15	0.69	11082	5907	2614	2316	245	R, S, P, CP, V
				Proportions [%]			
				C1/(A-C1)	**C2/(A-C1)**		
Mean (over areas)				13.1±8.5	16.2±29.1		
Mean (over all scatterers)				15.5	9.5		

*R: Residential zone
S: School district
P: Park
CP: Car park (outdoor)
A: Airport
V: Viaduct
B: Bridge

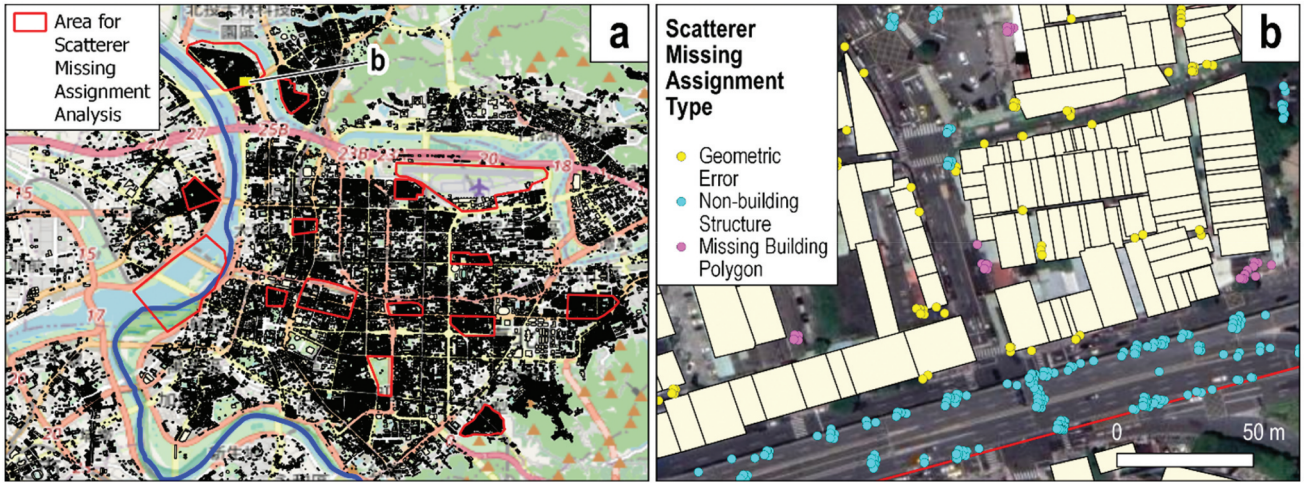

Figure A1. Scatterer assignment analysis. (a) Map showing areas (red polygons) chosen with relatively complete building polygons. (b) Examples of the three types of scatterer missing assignment.